Impact of oxygen release from bentonite on microbial activity, mineralogy, and steel corrosion

Natalia Jakus[1], Pranav Vivek Kulkarni[2], Carolin L. Dreher[3], Sylvie Bruggmann[4], Daniel Grolimund[5], Andreas Kappler[3], Nikitas Diomidis[6], Stefano Mischler[2], Rizlan Bernier-Latmani[1]

[1]Environmental Microbiology Laboratory, École Polytechnique Fédérale de Lausanne (EPFL), Switzerland
[2]Tribology and Interfacial Chemistry Group, École Polytechnique Fédérale de Lausanne (EPFL), Switzerland
[3]Geomicrobiology Group, University of Tübingen, Germany
[4]Institute of Earth Sciences, University of Lausanne, Switzerland
[5]Paul Scherrer Institute (PSI), Laboratory for Femtochemistry, Switzerland
[6]National Cooperative for the Disposal of Radioactive Waste (NAGRA), Switzerland

Contact addresses (in order):
#Corresponding author: natalia.jakus@epfl.ch
pranav.kulkarni@epfl.ch
carolin.dreher@uni-tuebingen.de
sylvie.bruggmann@unil.ch
daniel.grolimund@psi.ch
andreas.kappler@uni-tuebingen.de
nikitas.diomidis@nagra.ch
stefano.mischler@epfl.ch
rizlan.bernier-latmani@epfl.ch

Abstract

Deep geological repositories for the disposal of radioactive waste rely partly on the integrity of canisters and on the inhibition of microbial growth by the bentonite barrier for the effective isolation of the waste from the environment. Canister integrity can be compromised by the activity of sulfate-reducing bacteria (SRB) and by abiotic corrosion. Unexpected aerobic microbial growth and SRB inhibition under anoxic conditions were observed in bentonite during a recent long-term *in-situ* experiment. It raised the possibility that residual O_2 may delay anaerobic growth. Here, to investigate the role of O_2, bentonite was equilibrated with 0, 21, or 100% O_2, compacted to 1.25 g/cm³, and deployed in a borehole for 1.5 years. Analyses revealed that the higher the O_2 concentration in bentonite, the greater the biomass and the more *Desulfatitalea* sp. dominates the SRB population. The thickest corrosion layer product of carbon steel was found in the 21% O_2 case, reflecting ongoing aerobic and anaerobic processes. In contrast, the most extensive structural Fe(III) reduction within montmorillonite was observed at 0% O_2. These findings demonstrate that residual bentonite O_2 shapes microbial activity and alters corrosion dynamics, highlighting the importance of accounting for oxygen during early repository evolution.

Keywords: MX80, backfill, residual oxygen**,** anaerobic corrosion, aerobic corrosion, sulfate-reducing bacteria (SRB)**,** carbon steel**,** deep geological repository (DGR)

Synopsis: Residual oxygen in bentonite shapes microbial abundance and community structure, enhancing steel corrosion through abiotic and biotic processes under deep geological repository conditions.

Introduction

The long-term safety of deep geological repositories (DGRs) for radioactive waste relies on an engineered multi-barrier system designed to effectively isolate the waste from the surface.[1,2] The concept involves constructing tunnels in low-permeability rock hundreds of meters underground. In these tunnels, carbon steel (C-steel) canisters, like those proposed for Switzerland, will be surrounded by a bentonite buffer.[3] Wyoming bentonite MX80 is considered for its high montmorillonite content (up to 88 wt%) and its ability to retain radionuclides after canister failure.[4] Additionally, its swelling capacity upon contact with formation water gives it plasticity that reduces available pore space, thereby guaranteeing that the system remains diffusion-limited and bacterial activity is inhibited. Of particular concern for future DGRs, is the activity of sulfate-reducing bacteria (SRB), that use SO_4^{2-} sourced from the dissolution of sulfate minerals present in Wyoming bentonite (1.4 wt-%)[5] and porewater, and convert it to reduced S species, including HS^-. [6] This process can be fueled by a variety of electron donors[7], which in DGRs include gases such as CH_4 and H_2, and refractory solid organic matter (SOM) (*ca* 0.1 wt.% in Wyoming bentonite).[8–10] HS^- can then diffuse through the buffer towards the canisters, potentially leading to their corrosion, a process referred to as microbially induced corrosion (MIC).[11,12] MIC, alongside the abiotic aerobic and anaerobic corrosion processes expected post-DGR closure, can potentially compromise the long-term integrity of the canisters. In addition to the reduced S species they generate, SRB also have the potential for enzymatic Fe(III) reduction.[13–15] Fe^{2+}_{aq} released from corroding carbon steel can lead to recrystallization, transformation or reduction of some of the Fe(III)-bearing minerals present in bentonite, such as goethite (0.6 wt-%), lepidocrocite (0.9 wt-%), ilmenite, hematite, magnetite (ca. 0.1 wt-%)[16] and montmorillonite.[5,17–26] These changes may alter the porosity of the

buffer and, in the case of montmorillonite, could lead to the formation of secondary Fe(II)-bearing non-swelling clays e.g., illite, ultimately impairing buffer safety functions.[27–29]

However, the activity of SRB in the repository is expected to be constrained by factors such as the lack of space and substrate availability, low water activity, high temperature, or irradiation[12], but also, the presence of O_2 introduced during excavation of the repository. It is expected that anoxic conditions promoting SRB activity will develop within a few weeks to months post closure, once all O_2 has been depleted through e.g., abiotic oxidation of Fe(II) in mineral or metal components or the metabolic activity of aerobic heterotrophic bacteria.[30] However, a recent long-term *in-situ* incubation experiment under near-repository conditions demonstrated that, despite anoxic conditions, aerobic bacteria dominated the microbial community in Wyoming bentonite and there was no detectable contribution from SRB.[31] This unexpected result suggests that, while bulk O_2 has been removed, residual bentonite O_2–potentially associated with microporosity–supports the growth of aerobes while either directly or indirectly inhibiting that of SRB. However, the impact of bentonite-associated O_2 on the microbial community, and its influence on the mineralogical composition of bentonite and on the corrosion of bentonite-embedded steel remain unknown.

To address this knowledge gap, we systematically varied the O_2 concentration with which dry crushed Wyoming bentonite was equilibrated: 0, 21, and 100% O_2 (v/v). The bentonite was compacted to a density allowing for microbial growth and deployed into an anoxic borehole for 1.5 years. With a combination of molecular biology, chemistry, and mineralogical tools, we aimed to assess the impact of trapped O_2 on (1) microbial colonization, growth, and community composition, (2) mineralogical and chemical alterations in the bentonite backfill and (3) corrosion of carbon steel. The findings have significant implications for predicting post-closure conditions in waste deposition tunnels, offering new insights into microbial processes that may influence repository stability.

Materials and methods

Experimental Setup. Twelve stainless steel mini-modules (5.3 cm tall, 3.8 cm diameter) lined with sintered steel porous filters and filled with 1.25 g/cm^3 Wyoming MX-80 bentonite were placed into a larger module (25 cm tall, 12.6 cm diameter; Fig. S1) and incubated *in-situ* for 1.5 years in an anoxic borehole at the Mont Terri Underground Rock Laboratory (URL) in Switzerland. Prior to mini-module assembly, dry bentonite was ground to <3 mm and equilibrated for at least one year in (a) the absence of O_2 (hereafter, 0% O_2), (b) atmospheric O_2 (hereafter, 21% O_2), or (c) 100% O_2. In addition, gamma-irradiated (see SI) bentonite equilibrated with atmospheric O_2 (hereafter, 21%-S O_2) was included as a sterile control. Each mini-module contained carbon steel (C-steel) coupons (1.2 cm diameter, 0.3 cm thick; Amentum UK; Fig. S2), pre-cleaned to remove any initial corrosion products (SI). The bentonite O_2 desorption capacity into modified artificial porewater (APW) was confirmed in parallel batch tests using a FireSting-O_2 probe (Fig. S3).

Modules retrieval and bentonite sectioning. After removal from the borehole, the modules were packed under anoxic conditions (100% N_2), transported to the laboratory, and stored at 4°C. Next, using sterile tools, bentonite cores were removed from mini-modules and cut into three sections of 1.5-2.0 cm thickness (see SI) in a glovebox (100% N_2). Sections with coupons were resin-embedded (see SI), while the middle sections were subsampled to collect the inner part (2.51 cm diameter) and outer layer (a ring 1.29 cm thick). Samples for gDNA enumeration and sequencing were preserved at -20°C, and air- or freeze-dried for mineralogical characterization. More details can be found in the SI.

DNA extraction and quantification. DNA was extracted using previously published methods[32,33] following a modified protocol of DNeasy PowerMax Soil Kit (QIAGEN NV, Venlo, The Netherlands). Bentonite DNA was additionally purified by using 10 µL Invitrogen™Linear

Acrylamide (5 mg/mL), 0.1 volume of 5 M NaCl and 2 volumes of isopropanol. The air-dried DNA pellets were resuspended in 40 µL elution buffer provided in the DNeasy® PowerMax® Soil Kit and stored at -20°C. Extracted DNA was then quantified using an Invitrogen Qubit 2.0 fluorometer (see SI). For quantification of bacterial 16S rRNA gene copy numbers, quantitative PCR (qPCR) was performed using the MYRA robotic system and a MIC qPCR Cycler (both BioMolecular Systems, Australia). Reaction details and primer pair sequences are in the SI.

Sequencing and bioinformatics. The full-length 16S rRNA gene (V1-V9) amplicon libraries were prepared following the standard procedure from Pacific Biosciences of California, Inc. (aka PacBio) and sequenced using the Sequel II system. Raw reads were quality-checked using FASTQC (v0.11.9). Adapter trimming, quality filtering, dereplication, error modelling, and amplicon sequence variant (ASV) inference were conducted using DADA2 (v1.30.0). Taxonomic assignment was performed using the RDP naive Bayesian classifier against the SILVA SSURef database (v138). All analyses were run on the EPFL high-performance computing (HPC) cluster using SLURM (v23.11.10) and Apptainer (v1.2.5).

HCl and HF Fe extraction. Fe was extracted from freeze-dried powdered outer layers of cores and reference materials, which included bentonite (MX80), gamma-irradiated Wyoming bentonite (MX80-S), and chemically reduced Wyoming bentonite ($MX80_{red}$). The digestion was performed using either HCl (0.5 M or 6 M) to quantify readily available Fe, including adsorbed and solid-phase Fe(II) (e.g., siderite) or more crystalline phases (e.g. magnetite), or HF to quantify total Fe. All experiments were conducted in triplicate, and additional information on the digestion, analysis and chemical reduction of the clay are in the SI.

^{57}Fe Mössbauer spectroscopy. Mössbauer spectra collection was performed on freeze-dried powders at 77K using a close-cycle cryostat with a constant acceleration drive system (WissEL) in transmission mode with a ^{57}Co/Rh source. Spectral analysis was carried out using Recoil fitting

software (University of Ottawa) and the Voigt-Based Fitting (VBF) routine.[34] More details are available in the SI and Table S2.

X-ray diffractometry (XRD) Clay samples were freeze-dried and homogenized using a mortar. Non-oriented bulk samples were directly analyzed, while oriented mounts were processed to prepare air-dried, glycolated and heated (550°C; 1.5h) samples (SI). XRD was performed using X'Pert MPD with X'Celerate equipped with a Cu-anode (Cu Kα radiation, λ = 0.15406 nm). The resulting diffractograms were analyzed with Match! (version 3.6.2.121) and Crystallography Open Database (ver. COD-Inorg REV248644 2020.03.03).

X-ray Fluorescence (XRF) analysis. Maps of silicon (Si), sulfur (S) and iron (Fe; all K-edge) were obtained with an EDAX Orbis PCMicro EDXRF analyzer system (AMETEK Inc., Berwyn, Pennsylvania, U.S.A.), equipped with a Rh micro-focus X-ray tube at 12 and 20 keV acceleration and 0.9-1 mA current with 30 µm polycap optics and an Apollo XRF-ML50 Silicon Drift Detector. The spectra were recorded for 100-500 ms at each spot with a step size of 30 µm.

Bentonite water content. Bentonite water content and dry density were based on the wet weight loss after 24 hours of drying at 105°C following [35]. The dry weight of bentonite was used to normalize microbial and chemical data.

Corrosion analysis. The bentonite-coupon interface and the thickness of the corrosion product layer (CPL) were investigated using a Laser Confocal Optical Microscope (Keyence, VK-X200) with a Nikon objective (20x0.46, OFN25, WD-3.1 mm) in a depth composition mode. To calculate the CPL thickness, a minimum of 3 images at 20x and at least 30 measurements of CPL thicknesses were taken and analyzed by ImageJ. A Renishaw inViva Confocal Raman microscope, with a 532 nm laser and a 50X long-distance lens at optimum laser power in the range of 20 mW, was used to analyze the composition of CPL.

Mass loss and corrosion rates. The C-steel coupon mass was measured before the experiment and after removing corrosion products accumulated during incubation in the borehole. The products were chemically removed following the standard procedures [36], as described in SI.

Statistical analysis. ANOVA at alpha 0.05 determined significant treatment differences. For significant discrepancies, pairwise t-tests were performed with alpha 0.0083, adjusted via the Bonferroni correction method.

Results and discussion

Microbial growth in bentonite and adaptation to oxygen.

Quantification of microbial 16S rRNA gene copies confirmed growth in both the inner and outer parts of the bentonite core (Fig. 1A), with most of the growth happening in the outer layers. Significant differences ($p < 0.0083$) were observed between outer core growth between 0% O_2 and 21%-S O_2, 0% O_2 and 21% O_2, and 21%-S O_2 and 21% O_2. On average, the least growth could be quantified in the 0% O_2 treatment (4.16E+05 copies/gdw), while the most was found in the 100% O_2 case (1.93E+06 copies/gdw).

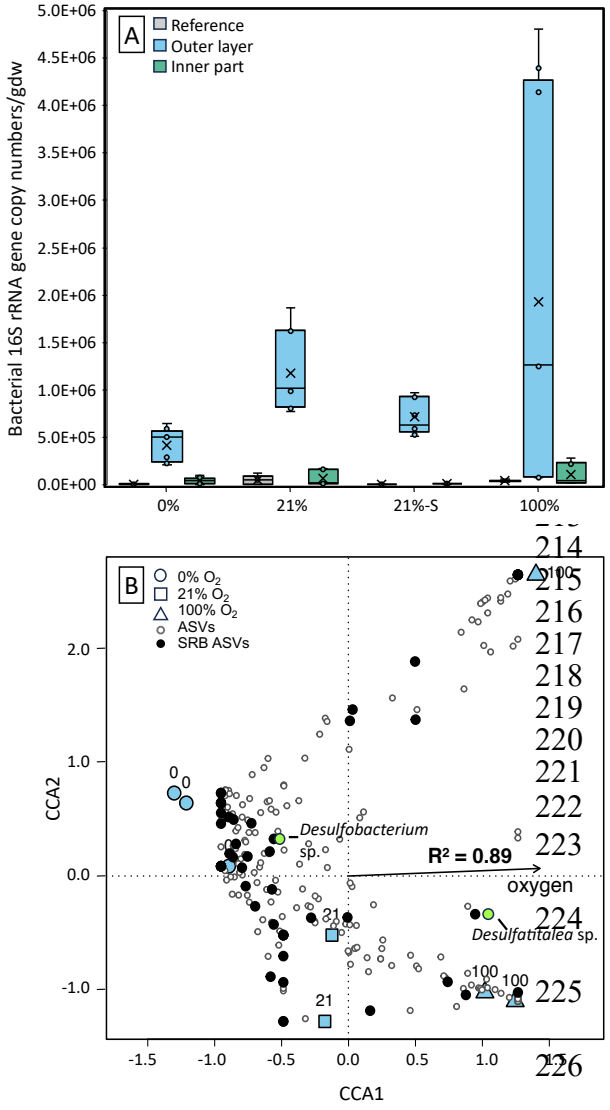

Figure 1. A: 16S rRNA gene V4 region amplicon copy numbers in bentonite before deployment (grey) and after 1.5 years *in-situ* incubation. Data differentiate gene copy numbers in the outer (green) and inner (blue) bentonite cores. The horizontal line in boxes indicates the median. 'X' marks the mean. Whiskers show minimum and maximum values outside the first and third quartiles. All results were standardized to the dry weight of bentonite. **B:** Canonical Correspondence Analysis (CCA) of microbial communities in the outer layer of the bentonite core, showing variation in relation to oxygen concentration with which bentonite was equilibrated before the deployment. Blue shapes represent the average for each treatment: 0% O_2 (circles), 21% O_2 (squares), and 100% O_2 (triangles). Each small circle represents an ASV; sulfate-reducing bacteria (SRB)-related ASVs are shown in black, with the two most abundant SRBs labeled and marked in neon green. The arrow indicates the direction and strength of the correlation between O_2 concentration and community composition.

Next, full-length 16S rRNA gene sequencing was used to determine microbial taxonomy of borehole and bentonite communities. (Fig. S4). The borehole water consortium was dominated by SRB (41.89±5.61% total relative abundance), with the highest relative abundance of two ASVs, with *Desulfobacterium* sp. (31.63±0.85%) and *Desulfatitalea* sp. (6.39±6.22; Fig. S5, Fig. S6). The rest of the SRB population consisted of *Desulfallas-Sporotomaculum* (0.76±0.18%), and other 110 ASVs. After SRB, the other most abundant genus was *Dethiobacter* sp. (27.12±3.81%) and two *Pseudomonas* spp. *P. xanthomarina* (19.83±6.71%) was previously reported in Opalinus Clay[37], while *P. stutzeri* (1.17±0.12%), a common facultative anaerobic bacterium, was previously found in compacted Wyoming bentonite in two long-term *in-situ* incubation studies.[31,32]

The bentonite outer layer samples showed high similarity to borehole communities with a few striking differences. First, the *Pseudomonas* spp. in bentonite represented, on average, 55.41±9.45% of the population. Second, *Dethiobacter* sp., being the second most abundant microorganism in borehole water, decreased in bentonite samples to merely 1.0±1.37%. Third, the overall SRB relative abundance in the bentonite outer layer was, on average, lower than in borehole water and depended on the bentonite O_2 equilibration concentration. Indeed, the relative abundance of the two most abundant SRB changed across treatments: *Desulfatitalea* sp. was the most abundant at 100% O_2, with 18.63±6.3 relative abundance vs. 0.94±1.01 at 0% O_2. Conversely, *Desulfobacterium* sp. had higher relative abundance at 0% O_2, at 18.90±8.50 vs. 3.98±3.12 at 100% O_2.

To investigate further the dependence of microbial abundance on O_2 concentration, the CCA was run on ASV counts from the outer part of bentonite cores (Fig. 1B). Almost all the separation among samples occurred along the O_2 gradient (CCA1 axis). Communities identified in 0% O_2 samples segregate sharply from those at 100% O_2, indicating that O_2 persisting in bentonite is the dominant factor structuring the communities. Microorganisms identified as related to SRB (black

circles) preferred but were not strictly limited to anoxia. Most SRB were found left of the zero line on the CCA1 axis, supporting their anaerobic niche. However, a subset of ASVs-SRB plots near/above zero, including the most abundant SRB, *Desulfatitalea* sp., indicating a possible adaptation of some SRB to grow in the presence of residual O_2.

Similar separation of ASVs depending on O_2 was observed for the inner core samples (Fig. S7). However, these microbial communities showed high diversity among replicates, most likely due to bias related to overall very low cell numbers, as demonstrated by the low number of gene copies and bentonite heterogeneity (Fig. 1A, Fig. S4). The communities were then screened for ASVs potentially involved in processes related to bentonite reduction or coupon corrosion, such as SO_4^{2-} reduction, Fe(III) reduction, Fe(II) oxidation, and H_2 oxidation (Fig. S8). Indeed, the SRB *Desulfatitalea* spp. was the most abundant in 100% O_2 samples. In addition, *Thiobacillus* spp., potentially involved in S oxidation and Fe(III) reduction were present in 0 and 21% O_2 samples, while potential H_2 oxidizers, e.g., *Hydrogenophaga* sp., were present under all conditions. Finally, *Acidovorax* sp., a potential Fe(II)-oxidizer, was found in 0% O_2 bentonite.

Taken together, these data demonstrate the growth of microbial communities inside compacted (1.25 g/cm^3) bentonite specifically responding to varying O_2 content, and present four lines of evidence for the ability of Opalinus Clay water bacteria to colonize bentonite. First, 16S rRNA gene copy numbers increased with respect to as-received bentonite and were much higher than the numbers in the inner core (Fig. 1A). Second, the community of bacteria in the outer layer strongly resembled but was not identical to borehole water (Figs. S4-S5). Third, the difference between the communities can be explained by the selectivity of bentonite as a habitat for some borehole water ASVs (e.g., *P. stutzeri and Dethiobacter* sp.). This is further supported by a previous study on granitic rock and bentonite MX80, which showed that some bacteria preferred the clay habitat within a repository setting (e.g., *Clostridia* spp.), while others were confined to groundwater (e.g.,

D. aespoeensis), and yet other bacterial lineages (e.g., *Sedimentibacter* and *Desulfosporosinus*) were found to live in both bentonite and groundwater.[38] Fourth, the positive correlation between copy numbers and O_2 (Fig. S9) indicates that microbial growth in bentonite was affected by O_2. This implies that bacteria grew inside the bentonite in an O_2-dependent manner. Altogether, the results support the colonization of bentonite but does not allow delineation of how far the colonization front progressed into bentonite due to the limited spatial resolution of the sampling. Our findings contrast with previous ones[31], in which no bentonite colonization was reported for the same borehole community. The discrepancy likely arises from differences in sample processing, whereby the outermost layer of the core, in direct contact with borehole water, was discarded.[31]

Finally, this study demonstrates the adaptation of some SRB to benefit from the presence of O_2 in bentonite, despite the fact that SRB are typically considered to be strict anaerobes.[39,40–42] More specifically, while most detected SRB species preferred bentonite with lower or no O_2, some favored growth in bentonite equilibrated with 100% O_2 (Fig. 1B). A striking example was the abundance of *Desulfatitalea* sp., whose relatives are known to inhabit deep subsurface sedimentary rocks (AY998140, query cover 100%, identity: 97.15%). In our study, *Desulfatitalea* sp. was found to be the most abundant in cores equilibrated with 100% O_2. We hypothesize that one reason for *Desulfatitalea* sp. remaining metabolically active might be its tolerance to the presence of O_2, which would allow it to outcompete less O_2-tolerant bacteria. Alternatively, it could have the ability to perform aerobic respiration, as documented for some SRB, including *Desulfurovibrio* species.[40] A third explanation is that the growth of *Desulfatitalea* sp. and other SRB in bentonite equilibrated with 100% O_2 is supported by metabolites (e.g., organic compounds) produced by aerobic microorganisms that potentially are the first ones to grow in this system, using residual O_2. These metabolites may have facilitated SRB growth that commenced after the depletion of O_2.

Solid phase analysis

HF and HCl extractions were performed on the outer core samples. The 0.5 M HCl extraction only yielded Fe(II) at a similar concentration across all samples (including the as-received MX80), an average of 1.95±0.32 mg/gdw of Fe(II) (Fig. 2, Table S1). The 6 M HCl extraction was used to access the pool of Fe associated with more crystalline phases and yielded an average of 7.00±0.47 mg/gdw of total Fe from all the samples, except 0% O_2 samples, which yielded a higher concentration (12.81 mg/gdw). Interestingly, a similar 6 M HCl-extractable total Fe (14.07-14.49 mg/gdw) can be obtained from MX80 chemically reduced by Na_2S or $Na_2S_2O_4$ (Table S1). Finally, HF was used for the quantification of total Fe and Fe(II) in the samples. The results showed that there was no significant difference in total Fe content between the samples ($p < 0.5$), on average reaching 23.38±1.67 mg/gdw, corresponding to 2.34±0.17 wt%. Therefore, the Fe data are compared and presented in terms of relative values (Fig 2; absolute values in Table S1). Fe(II) content varied between the samples, with the lowest content in the as-received MX80 yielding 10.10% of total Fe, while samples incubated in the borehole followed a general trend: the higher the O_2 content in the atmosphere before incubation, the less Fe(II) was present. 100% O_2 samples had 22.78% Fe(II), whereas 21% O_2 samples harbored 32.48% Fe(II), and 21%-S O_2 samples, 22.67% Fe(II). Finally, the highest Fe(II) concentration was found in 0 % O_2 bentonite, yielding 43.22% Fe(II).

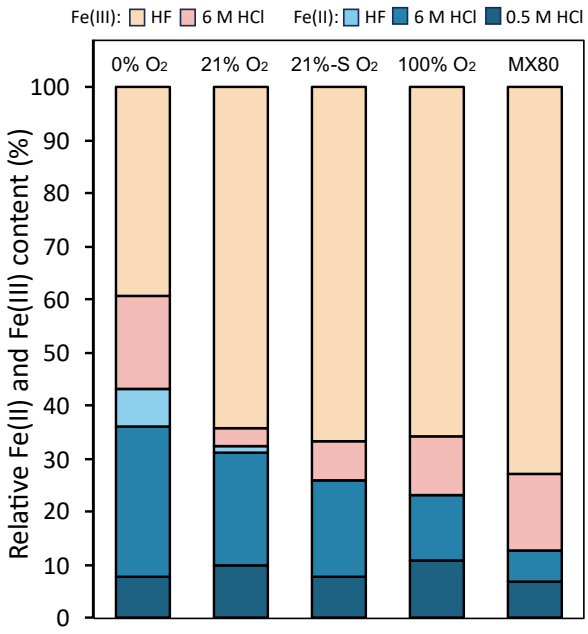

317

318 **Figure 2.** Fe(II) (blue) and Fe(III) (orange) extracted from bentonite outer cores after 1.5 years in a borehole, using
319 0.5 M HCl (readily available Fe), 6 M HCl (more crystalline phases), and HF (total Fe). Results were standardized to
320 g of Fe per dry weight of bentonite. HF-digested Fe was used as total Fe for calculating relative abundance of each
321 fraction.
322

323 X-ray diffraction (XRD) unveiled montmorillonite as a main clay component with a minor
324 contribution of illite in as-received MX80 (Fig. 3A, Fig. S9). Bentonite also contained feldspars
325 ($xAl(Al,Si)_3O_8$: orthoclase, sanidine), quartz (SiO_2), gypsum ($CaSO_4$), calcite ($CaCO_3$), goethite
326 (α-FeO(OH)) and pyrite (FeS_2), commonly found in MX80 (e.g, [5]). After *in-situ* incubation, new
327 phases like magnetite (Fe_3O_4) and siderite ($FeCO_3$) were formed only in the 0% O_2 sample
328 (Fig. S10). A stepwise procedure including glycolating and heating the oriented mounts showed no
329 montmorillonite alteration, such as formation of non-swelling clays (Fig. S11). Next, Mössbauer
330 spectroscopy was used to follow the fate of Fe in mineral phases. The spectra exhibited two Fe(II)
331 and two Fe(III) doublets, most likely stemming from octahedrally coordinated Fe in
332 montmorillonite, since all other Fe-bearing phases had too low relative content to generate a
333 detectable ^{57}Fe signal. The summed results confirmed the HF-extraction data showing an increase
334 in Fe(II) and a decrease in Fe(III) content as the O_2 content pre-incubation decreases (Table S3).

The as-received MX80 showed an overall Fe(III) content of 64.6%, while the Fe(III) in $MX80_{red}$ decreased to 30.6%. The 100% O_2 sample showed up to 68.65% Fe(III), while the 0% O_2 and 21% O_2 samples showed 48.6% and 55.7% Fe(III), respectively. The 21%-S O_2 sample exhibited 65.5% Fe(III), 10% more than its nonsterile equivalent (Fig. 3, Fig. S12, Table S3).

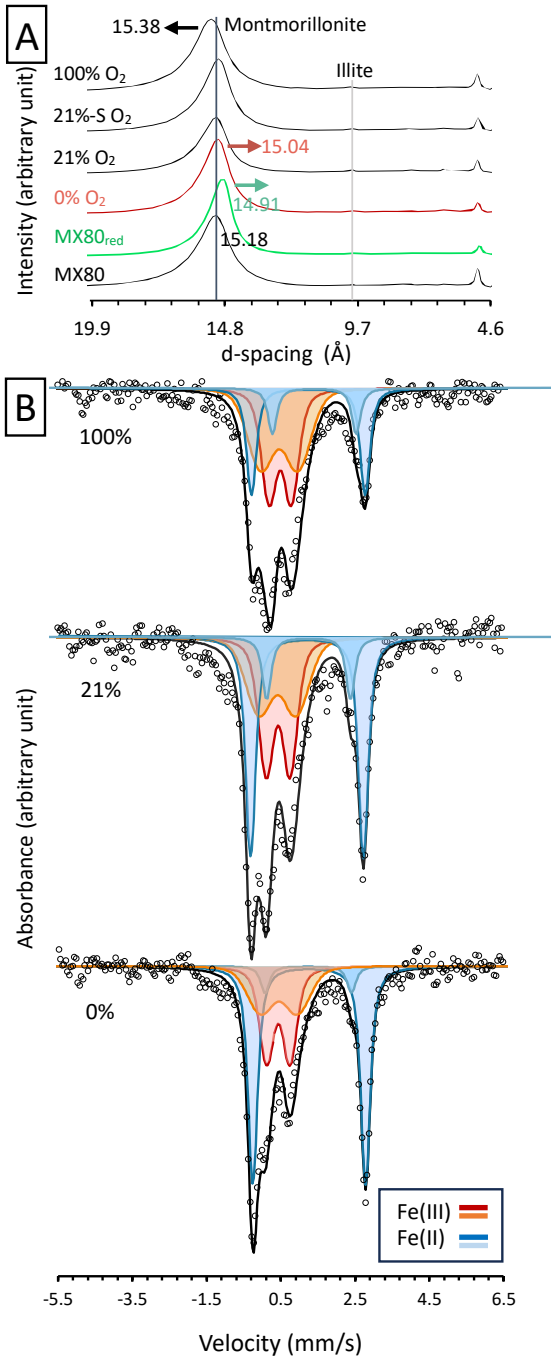

340

341 **Figure 3.** Mineralogical characterization of reference materials (MX80 and $MX80_{red}$) and samples after i*n-situ*
342 incubation. **A:** XRD patterns of randomly oriented bulk powders. Chemically reduced MX80 ($MX80_{red}$) is marked
343 with green. The vertical lines represent the position of the basal montmorillonite and illite reflections. Numbers above
344 the patterns show d-spacing values for montmorillonite. **B:** Mössbauer spectra (collected at 77 K) of 0% O_2, 21% O_2
345 and 100% O_2 samples after the *in-situ* incubation, showing an increase in the plot area related to the relative Fe(II)
346 content (blue doublets) and a decrease in the area representing Fe(III) (orange-red doublets) with decreasing O_2. Empty
347 circles represent raw data; the black line shows the fitted spectrum.
348

349

Micro X-ray Fluorescence (μXRF) analysis was used to map the distribution of Fe (Fig. S13) and S (Fig. 4) in the bentonite cores. Fe was used as an indicator of potential Fe phases, such as pyrite (FeS_2), siderite ($FeCO_3$) and iron sulfides (FeS_x) and Fe-containing clays (approximate montmorillonite formula $(Na,K,Ca)_{0.3}(Al,Mg,Fe,Ti)_2Si_4O_{10}(OH)_2 \cdot nH_2O$). Fe showed uniform distribution patterns reflecting the distribution of clays. Sulfur (S) was used to trace sulfate stemming from bentonite-derived gypsum ($CaSO_4 \cdot 2H_2O$) or FeS_x, present in the as-received bentonite, or formed during the *in-situ* incubation upon reduction of sulfate derived from porewater. S varied between samples, forming S-enriched bands of differing thicknesses (Fig. 4, Fig. S13). The 0% O_2 condition had the thickest layer (5.60±0.43 mm), while for 100% O_2 it measured only 0.46±0.1 mm. In summary, the less O_2, the thicker the S-enriched band in the outer layer, while Fe and Si remain evenly distributed across samples.

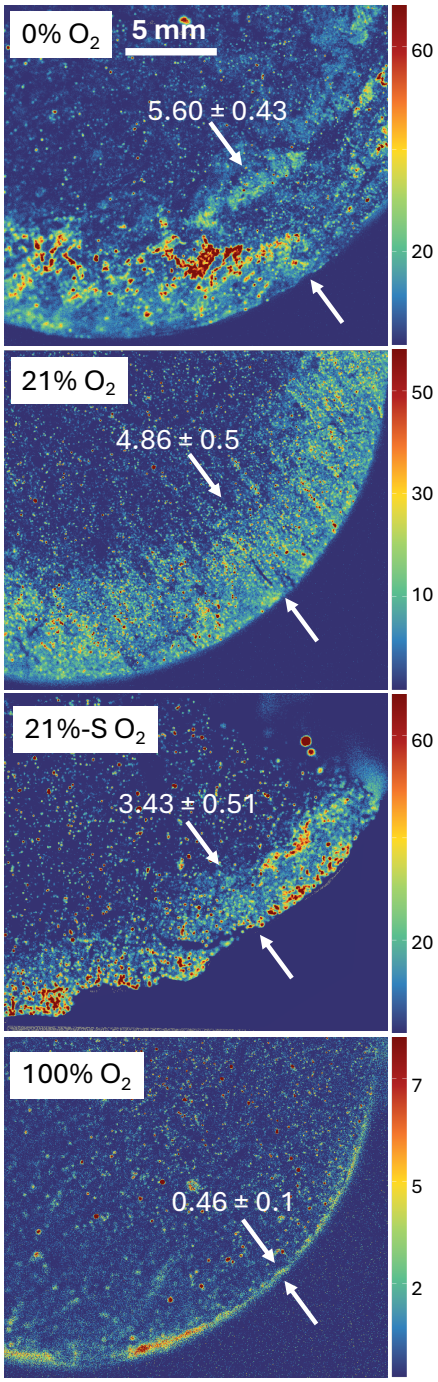

Figure 4: XRF elemental distribution maps of sulfur within the outer layer of the bentonite cores. Horizontal panels represent 0% O_2, 21%-S O_2, 21% O_2 and 100% O_2 bentonite treatments. The white arrows show the area enriched in S, reflecting the sulfate reduction front in the bentonite core in contact with sulfate-containing borehole water. Numbers show the thickness (n>30) of the band in mm.

Most of the Fe(III) reduction was observed in the 0% O_2 and the least in the 100% O_2 condition, providing direct evidence that the amount of associated O_2 is a controlling factor for the extent of

structural Fe(III) reduction in bentonite (Figs. 2&3). Furthermore, structural Fe(III) reduction in clay can be supported by three pieces of evidence. First, structural Fe in montmorillonite accounts for >90% of the total Fe in MX80, while other Fe-bearing minerals such as (oxyhydr)oxides or pyrite account for ≤5% of total Fe [41]. In 0% O_2, Fe(II) increased by 33.12%, compared to as-received MX80. Therefore, montmorillonite structural Fe(III) reduction must account for a large part of this increase. Second, the XRD data point to a shift of the basal smectite peak (001) to lower d-spacing values, consistent with the shift observed for chemically reduced montmorillonite ($MX80_{red}$). Third, Mössbauer spectra demonstrated the reduction of octahedral Fe(III) represented by two doublets identified as corresponding to montmorillonite, while the signal from other phases was not detected due to their low relative contribution. These findings indicate that Fe(III) reduction was facilitated by the depletion of sorbed O_2 due to: (i) the desorption and dissolution of O_2 after contact with anoxic borehole water, (ii) abiotic mineral oxidation, and/or (iii) biotic oxygen reduction.

In this system, bentonite Fe(III) can be reduced by Fe^{2+}_{aq} from anaerobic corrosion of C-steel, by the activity of SRB producing HS^-, and/or via direct enzymatic Fe(III) reduction by bacteria such as *Dethiobacter* sp. This bacterium was previously implicated in sulfur species disproportionation and thiosulfate reduction with H_2, as well as enzymatic Fe(III) reduction.[42,43] Additionally, Fe(III) reduction could be mediated by *Thiobacillus* spp., some species of which are known as Fe(III)-reducers [44]. Microbially mediated Fe(III) reduction was evidenced by HF-extracted Fe(II) content post-incubation for the 21% O_2 and 21%-S O_2 bentonite samples. For 21% O_2 samples, the Fe(II)/Fe(III) ratio was 45%, higher than that of the sterile one (ratio of 0.29), underscoring the role of microbial activity (Table S1). Further, the relative difference in Fe(II) content attributable to microbially driven Fe(III) reduction is most likely underestimated because a large portion of Fe(II) measured in the sterile control comes from reduction caused by gamma irradiation (50 kGy total

dose). A total dose of 40-60 kGy of radiation is expected to increase the Fe(II)/Fe(III) ratio in MX80 from ~0.1 to ~0.17-0.27[45] and the ratio in this study (after *in-situ* incubation) was 0.3 (Table S1), suggesting limited Fe(III) reduction in the irradiated bentonite.

Altogether, microbial growth and activity within bentonite were supported by a difference in microbial cell numbers, where an increase in abundance was observed across all samples. In addition, at 0% O_2, the growth was likely partly supported by metabolic processes involving S and Fe chemical species as electron acceptors, as the traces of O_2 that could be initially present were most likely rapidly depleted.

Corrosion analysis

Cross sections of the bentonite-coupon interface for all conditions revealed the following zonation based on the microscopic observations combined with elemental distribution collected with XRF (Fig. S14): (1) an unaltered C-steel coupon, (2) a corrosion product layer (CPL) covering the C-steel surface, (3) altered zone within bentonite, (4) unaltered bentonite. Across the samples, the thickness of CPL and altered zone differed significantly (Table S4) depending on the treatment. Among the non-sterilized bentonite samples, the lowest CPL thickness was 38.1±19.2 µm (0% O_2), while coupons placed within 21% O_2 or 100% O_2 bentonite were significantly thicker ($p < 0.05$): 121.5±79.7 µm and 96.5±33.9 µm, respectively. These values exceed those reported for the coupons in the previous *in situ* experiments in the same borehole.[46] However, the incubation time, dimensions of the modules, resin embedding method, and CPL thickness analysis method differed. The thickness of the altered zone exhibited the opposite trend to CPL, with the thickest layer measured for coupons in 0% O_2 bentonite (1.5±0.2 mm), while significantly lower values ($p < 0.05$) were measured for 21% O_2 or 100% O_2 bentonite (1.2±0.1 mm and 1.2±0.2 mm, respectively). The thickness measured for the 21% O_2 case was in agreement with the previous

studies, including the thickness of the FeOOH layer model predicted by a numerical simulation.[47] When comparing the non-sterilized and the gamma-sterilized bentonite samples, the sterilized sample exhibited significantly ($p < 0.05$) thinner CPL but thicker altered zone than the sample containing non-sterilized bentonite. Overall, in all comparisons between treatments, the following could be observed: the thicker the CPL, the thinner the altered zone layer, and vice-versa. Next, mass loss was used to quantify the average corrosion rates (Table S4). The calculated corrosion rates showed similar values for 0, 21, and 21%-S O_2 bentonite treatments: 2.50, 2.25, and 2.75 µm/year, in agreement with range of values published before[46], while 100% O_2 exhibited nearly double the corrosion rate: 4.25 µm/year. µRaman on the corrosion layer showed the presence of siderite, magnetite and goethite as the main products in all treatments (Fig. S15).

Progressive O_2 depletion is anticipated in the repository post-closure. This redox evolution will directly affect corrosion processes, including MIC, resulting in the formation of, first, oxic and then anoxic corrosion products on the canister-bentonite interface. When comparing 100% O_2 bentonite, where the activity of sulfate-reducing bacteria (SRB) was expected to be suppressed, to 0% O_2 bentonite, where SRB activity was expected to be enhanced, the CPL layer was significantly thicker in the former. Thus, the effects of abiotic O_2-driven corrosion outweighed the potential role of microbially driven corrosion. This indicates that, over a short timeframe, O_2-dependent corrosion may have a more substantial impact on the stability of the canister than microbial activity, even if the conditions are preferential (no O_2) for the activity of corrosion-inducing microorganisms. Given the inhibitory properties of high-density backfill (>1.45 g/cm³) and results from previous long-term (5.5 years) *in-situ* incubation experiments, where microbial growth in compacted bentonite was shown to be limited, and SRB abundance insignificant[31], MIC is not expected to contribute to the degradation of the canister, even after complete depletion of O_2.

The co-existence of reduced Fe(II)-bearing mineral phases (magnetite, siderite, reduced montmorillonite), and newly formed oxidized phases (e.g., goethite) in the altered zone associated with the coupons indicate that redox conditions during the incubation shifted from oxidizing to reducing. This transition occurred in all samples, regardless of the initial amount of bentonite-associated O_2, including 0% O_2 bentonite, most likely due to the traces of O_2 remaining in the bentonite (evidenced by the O_2 dissolution experiment (Fig. S3)).

O_2 evolution in DGRs: a conceptual model

Combining previous observations of C-steel corrosion in compacted bentonite[48–52] and the results from this study, the following model is proposed (Fig. S16 for illustration). First, starting from the coupon, aerobic corrosion of C-steel is initiated because of contact with water in bentonite and porewater entering the pores of bentonite. This leads to the formation of Fe(III) (oxyhydr)oxides (hematite or goethite/lepidocrocite[53]). As the corrosion layer thickens, direct contact of the Fe^0 in coupon with O_2 and H_2O progressively decreases, and the diffusion of O_2 from bentonite slows down, because of the growing layer and gradual depletion of O_2. Second, after O_2 in the near vicinity of the coupon is depleted, anaerobic corrosion of the C-steel starts, leading to the generation of Fe^{2+}_{aq}, which reduces previously formed (oxyhydr)oxides into magnetite, or forms siderite. The thickness of this CPL layer is dictated by the thickness of the primary (oxyhydr)oxide layer. Remaining Fe^{2+}_{aq} (not used in CPL formation) diffuses through the bentonite matrix and is oxidized by residual O_2 in the clay, where it precipitates forming the altered zone. This model is supported by the altered zone being thicker in samples initially equilibrated with an atmosphere containing only trace amounts of O_2 (i.e., 0% O_2 bentonite, Fig. S3) than those in 21 or 100 % O_2 samples. Indeed, a thinner altered zone is observed in the latter two, because most of the Fe^{2+}_{aq} released from C-steel was incorporated into the CPL or oxidized by O_2 in bentonite. Most of the

464 Fe(II) oxidation likely happens abiotically as microaerophilic Fe(II)-oxidizing bacteria have not
465 been identified in the samples, and other electron acceptors (e.g., nitrate) that could support
466 *Acidovorax* sp., a putative Fe(II)-oxidizer, are absent. In addition, the remaining Fe^{2+}_{aq} that did not
467 participate in the transformation or formation of new Fe(II) phases will reduce Fe(III) in minerals
468 such as goethite or montmorillonite, as supported by the acid digestion data. Fe(III) reduction in
469 clays may lead to retaining Fe(II) within the structure or reductive clay dissolution, causing the
470 formation of Al-Si gels. Si in contact with Fe^{2+} may further form Fe(II)-silicates, as previously
471 suggested[54], but these were not identified in this study
472 Redox changes at the bentonite-borehole water interface start from porewater entering the
473 bentonite, leading to immediate dissolution of bentonite-absorbed O_2, as demonstrated in the O_2
474 dissolution experiment (Fig. S3). Next, O_2 decreases due to its diffusion into the anoxic water,
475 microbial consumption mostly by borehole water bacteria such as *Pseudomonas* spp., and abiotic
476 reactions such as the oxidation of Fe(II) phases (e.g., pyrite) present in the as-received bentonite.
477 Next, microbial sulfate reduction commences, leading to the formation of sulfide. This sulfide can
478 reduce Fe(III)-bearing minerals (e.g., montmorillonite), react with reduced Fe^{2+}_{aq} (if present)
479 precipitating iron sulfide minerals (e.g., mackinawite), or react with residual O_2 to form
480 intermediate valence sulfur species that could be further used by SRB. Thus, the initial bentonite
481 O_2 content controls the extent of Fe(III) reduction, the S precipitation front, and the composition
482 of the microbial community via dictating the composition of SRB or Fe(III)-reducers.
483
484 *Environmental implications*
485 Our findings indicate that although future repository conditions are anoxic, O_2 will be initially
486 present and during a short period, will play a crucial role in controlling the abundance and
487 composition of microbial communities, Fe(III) reduction in bentonite, and C-steel corrosion. Here,

the initial presence of O_2 enhanced the growth of both indigenous bacteria and host rock bacteria that colonized bentonite. Surprisingly, this included SRB, particularly *Desulfatitalea* sp., even though this metabolic group is typically considered to be anaerobic. While result suggest microbial contribution to C-steel corrosion and alteration of bentonite, that contribution was less significant than abiotic reactions. Importantly, these findings were observed at a lower bentonite density (1.25 g/cm³) than the current minimum target density (1.45 g/cm³). Since dry density directly affects diffusion rates and microbial activity, higher-density scenarios in future repositories will further limit microbial-driven alteration, thereby reducing their overall impact. Thus, under the planned repository conditions, microbial processes are unlikely to pose a significant long-term threat to canister integrity or geochemical stability, despite the observed initial boost from O_2.

Data availability statement

Code and reproducible environments (Dockerfiles) for bioinformatic analysis are available here: https://github.com/nlmjacquemin/ICA6ANA2.

Acknowledgements

Niels Burzan helped with the experiment setup and deployment. Thanks to Nicolas Jacquemin for processing bioinformatic data, Pierre Rossi and EPFL Central Environmental Laboratory for qPCR results, and Wen Hua Bi and the Crystal Growth Facility for enabling XRD and XRF measurements. Martin Mazurek, Alina Hofer, and Frank Gfeller provided methods and advice on preparing and analyzing the oriented XRD mounts. Thanks to Manon Frutschi, Solexperts AG, Nagra and the Mont Terri Project Team for their support during fieldwork. This project has received funding from the European Union's Horizon 2020 research and innovation programme

under grant agreements N°847593 (EURAD) and N°101166718 (EURAD-2). SNF project Corint N°CRSII5_205883/1 supported Pranav Vivek Kulkarni.

References

(1) Ewing, R. C. Long-Term Storage of Spent Nuclear Fuel. *Nature Materials*. Nature Publishing Group 2015, pp 252–257. https://doi.org/10.1038/nmat4226.

(2) International Atomic Energy Agency. Status and Trends in Spent Fuel and Radioactive Waste Management Status and Trends in Spent Fuel and Radioactive Waste Management. *IAEA Nuclear Energy Series* **2022**.

(3) Design and Performance Assessment of HLW Disposal Canisters. NTB 24-20. *Nagra Technical Report* **2024**, *NTB 24-20*.

(4) Zeng, H.; Gonzalez-Blanco, L.; Romero, E.; Fraccica, A. The Importance of the Microstructure on Hydro-Mechanical Behaviour of Compacted Granular Bentonite. *Appl Clay Sci* **2023**, *246*. https://doi.org/10.1016/j.clay.2023.107177.

(5) Karnland, O. Chemical and Mineralogical Characterization of the Bentonite Buffer for the Acceptance Control Procedure in a KBS-3 Repository. *Svensk Kärnbränslehantering AB, Stockholm, Sweden* **2010**.

(6) Pedersen, K. State of Science on Microbiology in Radioactive Waste Disposal RNWMO0001. *Nuclear Waste Management Organization* **2018**.

(7) Plugge, C. M.; Zhang, W.; Scholten, J. C. M.; Stams, A. J. M. Metabolic Flexibility of Sulfate-Reducing Bacteria. *Front Microbiol* **2011**, *2* (MAY). https://doi.org/10.3389/fmicb.2011.00081.

(8) Wersin, P.; Stroes-Gascoyne, S.; Pearson, F. J.; Tournassat, C.; Leupin, O. X.; Schwyn, B. Biogeochemical Processes in a Clay Formation in Situ Experiment: Part G - Key Interpretations and Conclusions. Implications for Repository Safety. *Applied Geochemistry* **2011**, *26* (6), 1023–1034. https://doi.org/10.1016/j.apgeochem.2011.03.010.

(9) Cloet, V.; Pekala, M.; Smith, P.; Wersin, P.; Diomidis, N. An Evaluation of Sulphide Fluxes in the near Field of a HLW Repository. *Nagra Technical Report* **2017**, *NTB 17-04*.

(10) Maanoja, S.; Lakaniemi, A. M.; Lehtinen, L.; Salminen, L.; Auvinen, H.; Kokko, M.; Palmroth, M.; Muuri, E.; Rintala, J. Compacted Bentonite as a Source of Substrates for Sulfate-Reducing Microorganisms in a Simulated Excavation-Damaged Zone of a Spent Nuclear Fuel Repository. *Appl Clay Sci* **2020**, *196*. https://doi.org/10.1016/j.clay.2020.105746.

(11) Černoušek, T.; Ševců, A.; Shrestha, R.; Steinová, J.; Kokinda, J.; Vizelková, K. Microbially Influenced Corrosion of Container Material. In *The Microbiology of Nuclear Waste Disposal*; Elsevier, 2021; pp 119–136. https://doi.org/10.1016/b978-0-12-818695-4.00006-x.

(12) King, F. *Microbiologically Influenced Corrosion of Nuclear Waste Containers*; NACE International, 2008.

(13) Bale, S. J.; Goodman,', ' K; Rochelle, P. A.; Fry, J. R. J. C.; Weightman,' And, A. J. *Desulfovibrio Profundus Sp. Nov., a Novel Barophilic Sulfate-Reducing Bacterium from Deep Sediment Layers in the Japan Sea*; International Union of Microbiological Societies, 1997.

(14) Lentini, C. J.; Wankel, S. D.; Hansel, C. M. Enriched Iron(III)-Reducing Bacterial Communities Are Shaped by Carbon Substrate and Iron Oxide Mineralogy. *Front Microbiol* **2012**, *3* (DEC). https://doi.org/10.3389/fmicb.2012.00404.
(15) Lovley, D. R.; Roden, E. E.; Phillips, E.; Woodward, J. *Enzymatic Iron and Uranium Reduction by Sulfate-Reducing Bacteria*; 1993; Vol. 113.
(16) Karnland, O.; Olsson, S.; Nilsson, U.; Nuclear Fuel, S. Mineralogy and Sealing Properties of Various Bentonites and Smectite-Rich Clay Materials. *Svensk Kärnbränslehantering AB* **2007**.
(17) Handler, R. M.; Beard, B. L.; Johnson, C. M.; Scherer, M. M. Atom Exchange between Aqueous Fe(II) and Goethite: An Fe Isotope Tracer Study. *Environ Sci Technol* **2009**, *43* (4), 1102–1107. https://doi.org/10.1021/es802402m.
(18) Yong, S. N.; Lim, S.; Ho, C. L.; Chieng, S.; Kuan, S. H. Mechanisms of Microbial-Based Iron Reduction of Clay Minerals: Current Understanding and Latest Developments. *Applied Clay Science*. Elsevier Ltd October 1, 2022. https://doi.org/10.1016/j.clay.2022.106653.
(19) Rothwell, K. A.; Pentrak, M. P.; Pentrak, L. A.; Stucki, J. W.; Neumann, A. Reduction Pathway-Dependent Formation of Reactive Fe(II) Sites in Clay Minerals. *Environ Sci Technol* **2023**, *57* (28), 10231–10241. https://doi.org/10.1021/acs.est.3c01655.
(20) Liu, D.; Dong, H.; Bishop, M. E.; Zhang, J.; Wang, H.; Xie, S.; Wang, S.; Huang, L.; Eberl, D. D. Microbial Reduction of Structural Iron in Interstratified Illite-Smectite Minerals by a Sulfate-Reducing Bacterium. *Geobiology* **2012**, *10* (2), 150–162. https://doi.org/10.1111/j.1472-4669.2011.00307.x.
(21) Neumann, A.; Sander, M.; Hofstetter, T. B. *Redox Properties of Structural Fe in Smectite Clay Minerals*; 2011. https://pubs.acs.org/sharingguidelines.
(22) Wersin, P.; Hadi, J.; Jenni, A.; Svensson, D.; Grenèche, J. M.; Sellin, P.; Leupin, O. X. Interaction of Corroding Iron with Eight Bentonites in the Alternative Buffer Materials Field Experiment (ABM2). *Minerals* **2021**, *11* (8). https://doi.org/10.3390/min11080907.
(23) Joshi, P.; Fantle, M. S.; Larese-Casanova, P.; Gorski, C. A. Susceptibility of Goethite to Fe^{2+}-Catalyzed Recrystallization over Time. *Environ Sci Technol* **2017**, *51* (20), 11681–11691. https://doi.org/10.1021/ACS.EST.7B02603
(24) Notini, L.; Thomasarrigo, L. K.; Kaegi, R.; Kretzschmar, R. Coexisting Goethite Promotes Fe(II)-Catalyzed Transformation of Ferrihydrite to Goethite. *Environ Sci Technol* **2022**, *56* (17), 12723–12733. https://doi.org/10.1021/ACS.EST.2C03925
(25) Schikorr, G. Über Die Reaktionen Zwischen Eisen, Seinen Hydroxyden Und Wasser. *Zeitschrift für Elektrochemie und angewandte physikalische Chemie* **1929**, *35* (2), 65–70. https://doi.org/10.1002/BBPC.19290350204.
(26) Hofstetter, T. B.; Sosedova, Y.; Gorski, C.; Voegelin, A.; Sander, M. Redox Properties of Iron-Bearing Clays and MX-80 Bentonite-Electrochemical and Spectroscopic Characterization. *Nagra Technical Report* **2014**, *NTB 13-03*.
(27) Ohazuruike, L.; Lee, K. J. A Comprehensive Review on Clay Swelling and Illitization of Smectite in Natural Subsurface Formations and Engineered Barrier Systems. *Nuclear Engineering and Technology*. Korean Nuclear Society April 1, 2023, pp 1495–1506. https://doi.org/10.1016/j.net.2023.01.007.
(28) Cui, K.; Sun, S.; Xiao, M.; Liu, T.; Xu, Q.; Dong, H.; Wang, D.; Gong, Y.; Sha, T.; Hou, J.; Zhang, Z.; Fu, P. Microbial Mineralization of Montmorillonite in Low-Permeability Oil Reservoirs for Microbial Enhanced Oil Recovery. *Appl Environ Microbiol* **2018**, *84* (14). https://doi.org/10.1128/AEM.00176-18.

(29) Zhang, J.; Dong, H.; Liu, D.; Agrawal, A. Microbial Reduction of Fe(III) in Smectite Minerals by Thermophilic Methanogen Methanothermobacter Thermautotrophicus. *Geochim Cosmochim Acta* **2013**, *106*, 203–215. https://doi.org/10.1016/J.GCA.2012.12.031.

(30) King, F.; Kolàř, M.; Briggs, S.; Behazin, M.; Keech, P.; Diomidis, N. Review of the Modelling of Corrosion Processes and Lifetime Prediction for HLW/SF Containers—Part 1: Process Models. *Corrosion and Materials Degradation* **2024**, *5* (2), 124–199. https://doi.org/10.3390/cmd5020007.

(31) Burzan, N.; Lima, R. M.; Frutschi, M.; Janowczyk, A.; Reddy, B.; Rance, A.; Diomidis, N.; Bernier-Latmani, R. Growth and Persistence of an Aerobic Microbial Community in Wyoming Bentonite MX-80 Despite Anoxic in Situ Conditions. *Front Microbiol* **2022**, *13*, 1–12. https://doi.org/10.3389/fmicb.2022.858324.

(32) Engel, K.; Coyotzi, S.; Vachon, M. A.; McKelvie, J. R.; Neufeld, J. D. Validating DNA Extraction Protocols for Bentonite Clay. *mSphere* **2019**, *4* (5). https://doi.org/10.1128/msphere.00334-19.

(33) Vachon, M. A.; Engel, K.; Beaver, R. C.; Slater, G. F.; Binns, W. J.; Neufeld, J. D. Fifteen Shades of Clay: Distinct Microbial Community Profiles Obtained from Bentonite Samples by Cultivation and Direct Nucleic Acid Extraction. *Sci Rep* **2021**, *11* (1). https://doi.org/10.1038/s41598-021-01072-1.

(34) Lagarec, K.; Rancourt, D. G. Extended Voigt-Based Analytic Lineshape Method for Determining N-Dimensional Correlated Hyperfine Parameter Distributions in Mössbauer Spectroscopy. *Nucl Instrum Methods Phys Res B* **1997**, *129* (2), 266–280. https://doi.org/10.1016/S0168-583X(97)00284-X.

(35) *ISO 17892-1:2014 - Geotechnical investigation and testing — Laboratory testing of soil — Part 1: Determination of water content*. https://www.iso.org/standard/55243.html (accessed 2025-05-22).

(36) ASTM International. Standard Practice for Preparing, Cleaning, and Evaluating Corrosion Test Specimens. *Standard G1-03, ASTM Int., West Conshohocken, PA, USA.* **2017**.

(37) Bagnoud, A.; Chourey, K.; Hettich, R. L.; De Bruijn, I.; Andersson, A. F.; Leupin, O. X.; Schwyn, B.; Bernier-Latmani, R. Reconstructing a Hydrogen-Driven Microbial Metabolic Network in Opalinus Clay Rock. In *Nature Communications*; Nature Publishing Group, 2016; Vol. 7. https://doi.org/10.1038/ncomms12770.

(38) Chi Fru, E.; Athar, R. In Situ Bacterial Colonization of Compacted Bentonite under Deep Geological High-Level Radioactive Waste Repository Conditions. *Appl Microbiol Biotechnol* **2008**, *79* (3), 499–510. https://doi.org/10.1007/s00253-008-1436-z.

(39) Rabus, R.; Hansen, T. A.; Widdel, F. Dissimilatory Sulfate- and Sulfur-Reducing Prokaryotes. In The Prokaryotes. E. Rosenberg, E.F. DeLong, S. Lory, E. Stackebrandt, and F. Thompson (Eds). Berlin Heidelberg: Springer, Pp. 309–40. In *In The Prokaryotes*; Rosenberg, E., DeLong, E. F., Lory, S., Stackebrandt, E., Thompson, F., Eds.; Springer: Berlin Heidelberg, 2013; pp 309–404.

(40) Cypionka, H. Oxygen Respiration by Desulfurovibrio Species. *Annu. Rev. Microbiol.* **2000**, *54*, 827–848.

(41) Wersin, P.; Hadi, J.; Jenni, A.; Svensson, D.; Grenèche, J.-M.; Sellin, P.; Leupin, O. X.; Kalinichev, G. Minerals Interaction of Corroding Iron with Eight Bentonites in the Alternative Buffer Materials Field Experiment (ABM2). **2021**. https://doi.org/10.48350/164965.

(42) Sorokin, D. Y.; Tourova, T. P.; Mußmann, M.; Muyzer, G. Dethiobacter Alkaliphilus Gen. Nov. Sp. Nov., and Desulfurivibrio Alkaliphilus Gen. Nov. Sp. Nov.: Two Novel Representatives of Reductive Sulfur Cycle from Soda Lakes. *Extremophiles* **2008**, *12* (3), 431–439. https://doi.org/10.1007/s00792-008-0148-8.

(43) Zavarzina, D. G.; Merkel, A. Y.; Klyukina, A. A.; Elizarov, I. M.; Pikhtereva, V. A.; Rusakov, V. S.; Chistyakova, N. I.; Ziganshin, R. H.; Maslov, A. A.; Gavrilov, S. N. Iron or Sulfur Respiration—an Adaptive Choice Determining the Fitness of a Natronophilic Bacterium Dethiobacter Alkaliphilus in Geochemically Contrasting Environments. *Front Microbiol* **2023**, *14*. https://doi.org/10.3389/fmicb.2023.1108245.

(44) Suzuki, I.; Takeuchi, T. L.; Yuthasastrakosol, T. D.; Oh, J. K. Ferrous Iron and Sulfur Oxidation and Ferric Iron Reduction Activities of Thiobacillus Ferrooxidans Are Affected by Growth on Ferrous Iron, Sulfur, or a Sulfide Ore. *Appl Environ Microbiol* **1990**, *56* (6), 1620–1626. https://doi.org/10.1128/AEM.56.6.1620-1626.1990.

(45) Holmboe, M. Effect of Gamma-Irradiation on the Redox States of the Structural Iron in Bentonite Clay. **2023**.

(46) Reddy, B.; Padovani, C.; Smart, N. R.; Rance, A. P.; Cook, A.; Milodowski, A.; Field, L.; Kemp, S.; Diomidis, N. Further Results on the in Situ Anaerobic Corrosion of Carbon Steel and Copper in Compacted Bentonite Exposed to Natural Opalinus Clay Porewater Containing Native Microbial Populations. *Materials and Corrosion* **2021**, *72* (1–2), 268–281. https://doi.org/10.1002/MACO.202011785.

(47) Leupin, O. X.; Smart, N. R.; Zhang, Z.; Stefanoni, M.; Angst, U.; Papafotiou, A.; Diomidis, N. Anaerobic Corrosion of Carbon Steel in Bentonite: An Evolving Interface. *Corros Sci* **2021**, *187*, 109523. https://doi.org/10.1016/J.CORSCI.2021.109523.

(48) Wersin, P.; Hadi, J.; Kiczka, M.; Jenni, A.; Grenèche, J. M.; Diomidis, N.; Leupin, O. X.; Svensson, D.; Sellin, P.; Reddy, B.; Smart, N.; Zhang, Z. Unravelling the Corrosion Processes at Steel/Bentonite Interfaces in in Situ Tests. *Materials and Corrosion* **2023**, *74* (11–12), 1716–1727. https://doi.org/10.1002/MACO.202313755.

(49) Leupin, O. X.; Smart, N. R.; Zhang, Z.; Stefanoni, M.; Angst, U.; Papafotiou, A.; Diomidis, N. Anaerobic Corrosion of Carbon Steel in Bentonite: An Evolving Interface. *Corros Sci* **2021**, *187*, 109523. https://doi.org/10.1016/J.CORSCI.2021.109523.

(50) Ishidera, T.; Ueno, K.; Kurosawa, S.; Suyama, T. Investigation of Montmorillonite Alteration and Form of Iron Corrosion Products in Compacted Bentonite in Contact with Carbon Steel for Ten Years. *Physics and Chemistry of the Earth, Parts A/B/C* **2008**, *33* (SUPPL. 1), S269–S275. https://doi.org/10.1016/J.PCE.2008.10.062.

(51) Carlson, L.; Karnland, O.; Oversby, V. M.; Rance, A. P.; Smart, N. R.; Snellman, M.; Vähänen, M.; Werme, L. O. Experimental Studies of the Interactions between Anaerobically Corroding Iron and Bentonite. *Physics and Chemistry of the Earth, Parts A/B/C* **2007**, *32* (1–7), 334–345. https://doi.org/10.1016/J.PCE.2005.12.009.

(52) Kozaki, T.; Imamura, Y.; Takada, J.; Sato, S.; Ohashi, H. Corrosion of Iron and Migration of Corrosion Products in Compacted Bentonite. *Materials Research Society Symposium - Proceedings* **1995**, *353* (1), 329–336. https://doi.org/10.1557/PROC-353-329/METRICS.

(53) Wersin, P.; Hadi, J.; Kiczka, M.; Jenni, A.; Greneche, J.-M.; Diomidis, N.; Leupin, O. X.; Svensson, D.; Sellin, P.; Bharti, R.; Smart, N.; Zhang, Z. Unravelling the Corrosion Processes at Steel/Bentonite Interfaces in in Situ Tests. *Materials and Corrosion* **2023**, *74* (11–12), 1716–1727.

(54) Kaufhold, S.; Klimke, S.; Schloemer, S.; Alpermann, T.; Renz, F.; Dohrmann, R. About the Corrosion Mechanism of Metal Iron in Contact with Bentonite. *ACS Earth Space Chem* **2020**, *4* (5), 711–721.

Supplementary information

Impact of oxygen release from bentonite backfill on microbial activity, bentonite mineralogy and canister corrosion

Natalia Jakus[1], Pranav Vivek Kulkarni[2], Carolin L. Dreher[3], Sylvie Bruggmann[4], Daniel Grolimund[5], Andreas Kappler[3], Nikitas Diomidis[6], Stefano Mischler[2], Rizlan Bernier-Latmani[1]

[1]Environmental Microbiology Laboratory, École Polytechnique Fédérale de Lausanne (EPFL), Switzerland
[2]Tribology and Interfacial Chemistry Group, École Polytechnique Fédérale de Lausanne (EPFL), Switzerland
[3]Geomicrobiology Group, University of Tübingen, Germany
[4]Institute of Earth Sciences, University of Lausanne, Switzerland
[5]Paul Scherrer Institute (PSI), Laboratory for Femtochemistry, Switzerland
[6]National Cooperative for the Disposal of Radioactive Waste (NAGRA), Switzerland

#Corresponding author: natalia.jakus@epfl.ch

Number of pages: **20**
Number of figures: **16**
Number of tables: **4**

1. Supplementary methods

Gamma irradiation of bentonite. The gamma-irradiated bentonite served as a sterile control. For sterilization, Wyoming MX-80 bentonite was placed in an anoxic Schott bottle, flushed with N_2, and sealed with a rubber septum. A minimum dose of 50 kGy was applied using a Cobalt-60 source at Wood PLC in Harwell, Oxfordshire, UK, and stored in the sealed bottle until the module assembly. Note that even though gamma irradiation is the most effective sterilization method for rock powders and induces minimal changes, it can affect relevant bentonite properties, including Fe(III) reduction, water content, and carbon speciation. Consequently, redox processes, microbial activity, or diffusion rates can be affected. Thus, while it is the best control available, it is not perfect and, thus, does not allow for a complete comparison of the two materials (21% O_2 and 21%-S O_2).

Removal of the initial corrosion products from the coupon surface before emplacement. C-steel coupons underwent sequential washing steps using (1) 1.2 M HCl, (2) anoxic MQ, and (3) methanol to remove corrosion products. For each washing step, the coupons were placed in a flask with the solution and submerged in an ultrasonic bath for 10-30 min. The final washing step was followed by drying under a continuous flow of N_2, and the coupons were stored under anoxic conditions until the mini-modules were assembled.

The desorption batch experiment. The O_2 desorption capacity of bentonite upon contact with artificial porewater (modified APW, [1]) was confirmed in a separate O_2 dissolution experiment, in which the three bentonite powders (1 g each) were suspended in individual serum bottles containing 57 mL of anoxic APW (no gaseous headspace), and aqueous O_2 release was monitored (Fig S3) using a fiber-optic meter (FireSting-O_2, PyroScience GmbH, Aachen, Germany).

Modules retrieval and bentonite sectioning. After incubation, the module containing twelve mini-modules was retrieved from the borehole and immediately transferred to the anoxic glovebox (100% N_2) available at the site (Niche MA, Mont Terri URL). In the glovebox (100% N_2), the mini-modules were removed from the module and packed into Mylar® bags. Bags were then removed from the glovebox, transported to the laboratory and stored at 4°C until processing. The bentonite cores were recovered from the mini-modules using a sterile lever press (in an ambient atmosphere) and sectioned under sterile and anoxic conditions (100% N_2 glovebox). Each core was cut into three slices (1.5-2.0 cm thickness); two containing the steel coupons and the middle one without a coupon (Fig S2). Maintaining anoxic conditions, the sections containing coupons were resin-embedded (SI) for corrosion characterization, while the middle sections of the cores were further sectioned using a sterile cylindrical tool to collect samples representing the inner part of the core (2.51 cm diameter) and the outer layer (a ring of 1.29 cm thickness), and preserved at -20° C for gDNA enumeration, and air-, or freeze-dried under anoxic conditions for mineralogical characterization.

Bentonite resin embedding for coupon-bentonite interface analysis. C-steel coupons, contained within bentonite sections measuring 1.5 to 2.0 cm in thickness, were sealed inside Mylar® bags within a glovebox (100% N_2) to ensure anoxic conditions. The samples were then frozen at -20°C and freeze-dried overnight. Dried samples were immediately transported to an anoxic glovebox. All next steps were then performed in the glovebox. First, EPO-TEK® 301-2, a two-component epoxy resin with low viscosity equilibrated with the glovebox atmosphere, was prepared according to the manufacturer's instructions for embedding the coupons. Silicone molds were coated with Vaseline® to enable the later removal of the resin. Next, a thin layer (approximately 3-4 mm) of resin was poured into the bottom of each mold and allowed to harden overnight. The next day, the freeze-dried samples were placed on top of this layer and covered with another portion of freshly prepared resin, with an excess applied to create a top layer of approximately 3-4 mm. The molds containing resin-embedded samples were then placed inside a desiccator connected to a pump. At least five vacuum-refill (N_2) cycles were conducted to remove all gas bubbles from bentonite, ensuring the resin penetrated the available pore spaces. Following this process, the samples were left to harden in the glovebox at least 48 hours. Finally, the resin-embedded bentonite samples containing the coupons were removed from the molds. They were

then dry-cut using a saw under oxic conditions. After cutting, the samples were stored anoxically to limit O_2 exposure.

DNA quantification using a fluorometer. Extracted DNA was quantified using an Invitrogen Qubit 2.0 fluorometer with 2 µL of extracted DNA and 198 µL of a working solution prepared by mixing Qubit™ buffer solution and fluorescent Qubit™ reagent following the standard protocol provided by the manufacturer.

16S rRNA gene copy quantification using qPCR. Quantitative PCR (qPCR) of bacterial 16S gene copy numbers was performed using the MYRA robotic system and a MIC qPCR Cycler (both BioMolecular Systems, Australia) using10 µL reactions in triplicates. For quantification of gene abundance, the following volumes of substrates were used: 2.5 µL template DNA, 2.1 µL water, 0.2 µL of each primer (100 mM stock) and 5 µL of 2× SensiFAST SYBR ® No-ROX Kit (Meridian Bioscience, UK). Samples were cycled (40 cycles) at 95 °C for 5 s, followed by an extension at 62 °C for 10 s and the acquisition at 72 °C for 5 s. The final melting step was carried out from 72 °C to 95 °C, at a rate of 0.1 °C/s. Analysis of the results was performed using the built-in analytical software (micPCR, BioMolecular Systems, ver. 2.12.6). Average efficiency (0.943 – 1.003) and r^2 values (> 0.99) were determined from seven points of the serial dilutions (10^7 –10^1 copies) for bacterial 16S rRNA gene. Based on calibration curves obtained using *E. coli* DNA, C_q values were used to calculate the gene copy numbers which were normalized against the mass (ng) of the extracted DNA. The primer pair used for the reaction to quantify bacterial 16S rRNA gene consisted of 338f: 5'-ACT CCT ACG GGA GGC AGC AG-3' and 534r: 5'-ATT ACC GCG GCT GCT GGC A-3'.

HCl and HF Fe extraction. The freeze-dried outer layers of the cores, together with the reference materials (Wyoming bentonite (MX80), and gamma-irradiated Wyoming bentonite (MX80-S)) were subjected to HCl extractions to quantify and distinguish between different Fe pools. 0.5 M HCl is typically used to solubilize adsorbed and solid phase Fe(II) species, including siderite and green rust, and the reactive fraction of Fe(III) minerals [2], while 6 M HCl is used to extract more crystalline iron phases such as poorly reactive sheet silicate Fe or FeS species [3,4] Before extractions, all glassware was kept in a 10% HCl bath overnight and rinsed 3x with distilled water and 3x with MilliQ water. In an anoxic glovebox (100% N_2), 0.5 g of dry clay was weighed into a 50 mL serum bottle with 10 mL extractant and N_2 headspace. Throughout the extraction, all samples were kept in the dark for 24 h under anoxic conditions. Samples extracted with 0.5 M HCl were continuously shaken on a horizontal shaker at 100 rpm at room temperature, while samples mixed with 6 M HCl were kept anoxically in a 70 °C water bath. Following the extraction, 1 mL of sample was collected inside the glovebox at room temperature for 5 min at 13'500×g centrifugation, and 20 µL of supernatant was collected for 50x dilution in anoxic 1 M HCl. Fe(II) was quantified using the Ferrozine assay.[5] The concentration of Fe(III) was calculated by subtracting Fe(II) from total Fe. Total Fe was obtained by HF digestions and quantified using the 1,10-phenanthroline assay as described earlier[6]. All experiments were performed in triplicate.

Preparation and handling of dithionite-reduced smectite suspensions. A 30 mM solution of Na_2S and a 30 mM solution of $Na_2S_2O_2$ were used to prepare the reference material of chemically reduced MX80 ($MX80_{red}$) following the method adapted from [7,8]. Briefly, in an anoxic glovebox (100% N_2), 1 g of powdered bentonite was suspended in 5 mL of citrate-bicarbonate buffer, and 30 mM of either Na_2S or 30 $Na_2S_2O_2$ was added. The vials were crimped to maintain anoxic conditions and allowed to react for 30 minutes in a 70°C water bath. Afterwards, the vials were brought back to the glovebox, and the supernatant, along with the particles, were transferred to several centrifugation tubes and centrifuged to remove the supernatant. The resulting reduced clay was washed with anoxic MQ in several (minimum 3) washing-centrifugation steps to remove residues of the salts from the supernatant and allowed to air-dry inside the glovebox. After drying, the powder was transferred to a vial and stored anoxically.

^{57}Fe Mössbauer Spectroscopy. Dried mineral powders were loaded into Plexiglas holders (area 1 cm^2), forming a thin disc. Holders were inserted into a closed-cycle exchange gas cryostat (Janis Cryogenics; now Lake Shore Cryotronics, Inc.) under a backflow of Helium to minimize exposure to air. Spectra

were collected at 77K and 5K using a constant acceleration drive system (WissEL) in transmission mode with a ^{57}Co/Rh source. All spectra were calibrated against a 7 μm μm-thick α-^{57}Fe foil that was measured at room temperature. Analysis was carried out using Recoil fitting software (University of Ottawa) and the Voigt Based Fitting (VBF) routine.[9] The half width at half maximum (HWHM) was constrained to 0.124 mm/s during fitting.

Preparation of oriented samples for XRD analysis. Non-oriented samples were directly analyzed, while oriented mounts were prepared by deflocculation and decalcification of the bentonite sample, followed by slow sedimentation on a glass slide, allowing for the orientation of the clay crystals. Three oriented mounts were prepared for each sample: (1) air-dried, (2) glycolated, prepared by overnight incubation in a desiccator with an ethylene glycol-saturated atmosphere at 50°C, and (3) heated; prepared by heating the air-dried oriented sample up to 550°C for 1.5h.

Corrosion analysis. The interface of metal coupons and bentonite, along with the thickness and specific features of the corrosion product layer (CPL), was investigated using a Laser Confocal Optical Microscope Keyence (VK-X200) in depth composition mode, equipped with a Nikon objective (20x0.46, OFN25, WD-3.1 mm). To calculate the CPL thickness, a minimum of 3 images at 20x and at least of 30 measurements of CPL thicknesses were taken and analyzed with ImageJ software.[10] The Renishaw inViva Confocal Raman microscope with 532 nm laser and a 50X long-distance lens at optimum laser power in the range of 20 mW, was used to analyze the composition of the CPL.

Mass loss and corrosion rates. The C-steel coupon mass was measured before the experiment and after removing corrosion products accumulated during incubation in the borehole. The products were chemically removed following the standard procedures [11]. The dismantled coupons were washed with acetone in the ultrasonication for 2 minutes as a pre-step to remove loosely bound attached material/products. Thereafter, coupons were ultrasonically stirred in the solution containing 12.08 M HCl, 0.069 M Sb_2O_3 and 0.26 M $SnCl_2$ at room temperature for 2 minutes. The procedure was repeated until the weight of the coupons did not change between the cleaning steps. The corrosion rate was calculated as described below.

Corrosion rate calculations. The initial total surface area of the C-steel coupons delivered by Jacobs Engineering (Harwell Campus, UK; formerly Wood, AMEC Foster Wheeler) was recorded before the assembly of the modules. After the retrieval of the samples from the borehole, the mass loss was determined by subtracting the coupons' weight after removing corrosion products following the standard procedure (Methods), from the initial weight. The average corrosion rate was obtained as follows:

$$\text{Corrosion Rate} = (K \times W / A \times T \times D)$$

where:

K – corrosion constant (mm/year) = 8.76×10^4 mm/year
T – exposure time (h) = 13140 h
A – coupon areas (cm^2) = 3.39 cm^2
W – mass loss (g)
D – C-steel density (g/ cm^3) = 7.86 g/ cm^3

2. Supplementary figures

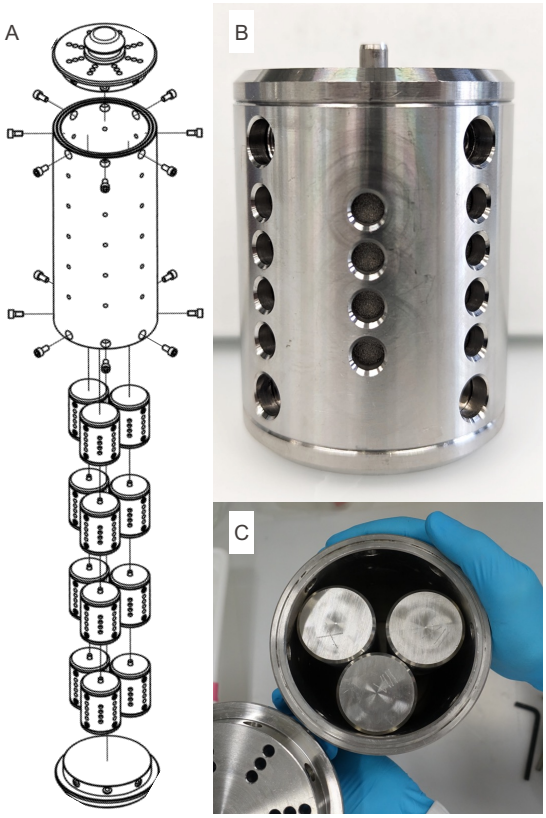

Figure S1. Experimental set-up**. A:** Technical drawing of a perforated stainless steel module housing 12 individual mini-modules. **B:** Photograph showcasing a single mini-module**. C:** Top view illustrating the arrangement of three mini-modules within the larger module.

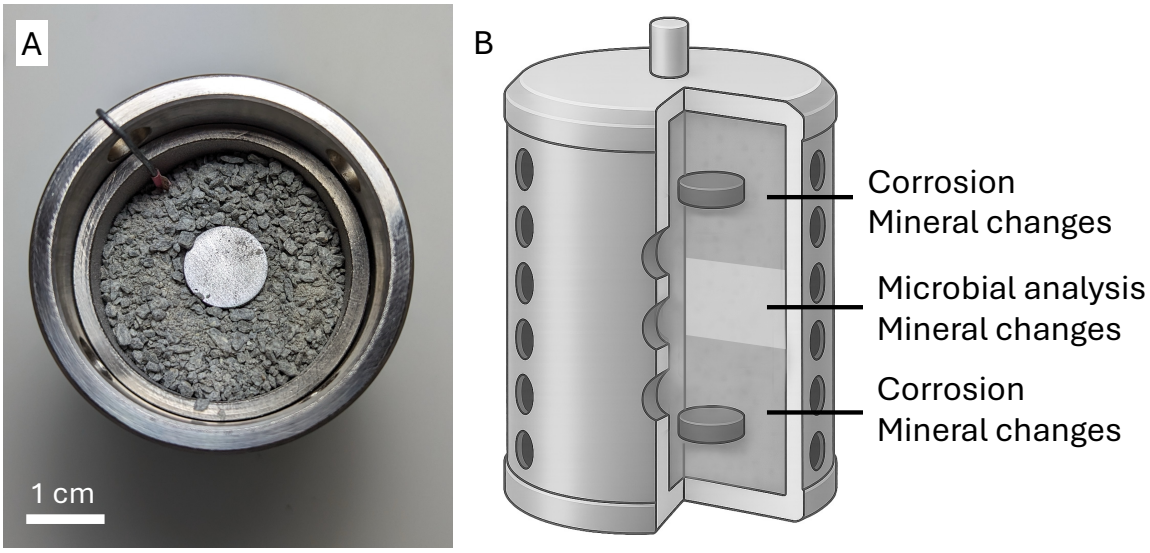

Figure S2. Assembly of the mini-module. **A:** Top view illustrating the mini-module filled with bentonite particles and the coupon placed in the middle. **B:** Mini-module diagram showing the placement of metal coupons and sectioning pattern: the coupon-containing layers (top and bottom) were used for studying the coupon-bentonite interface and corrosion, while the middle section was designated for microbial analysis (quantification and taxonomy identification) and mineral changes.

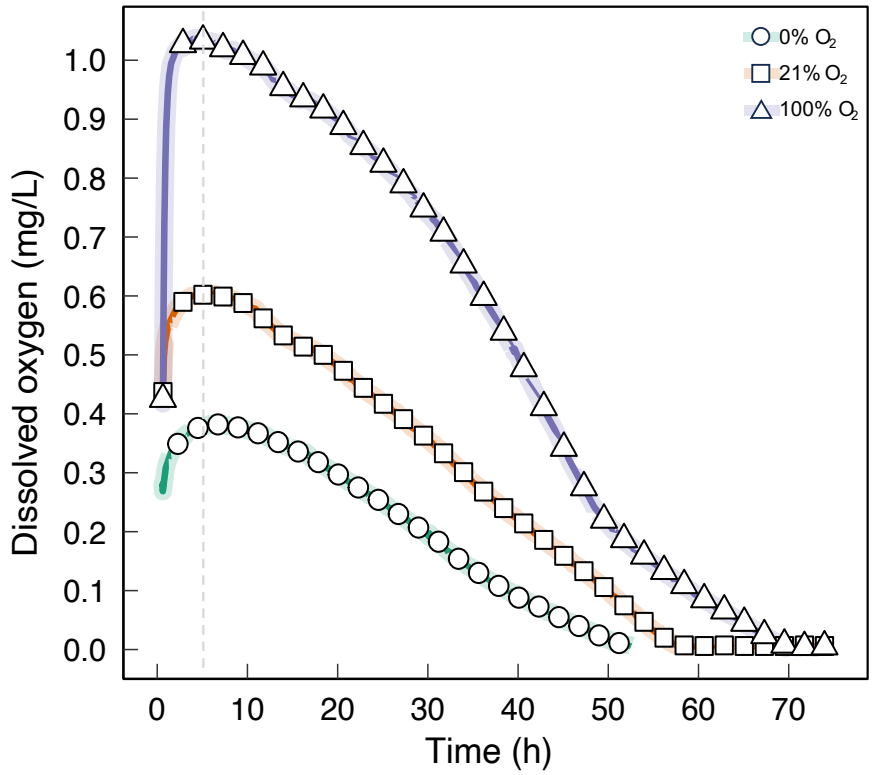

Figure S3. Oxygen dissolution in artificial pore water (APW) upon contact of bentonite equilibrated with 0% O_2 (green), 21% O_2 (orange) and 100% O_2 (purple) - containing atmosphere before *in-situ* incubation in the borehole (reference materials). The dashed vertical line represents the time needed for the maximum desorption of oxygen.

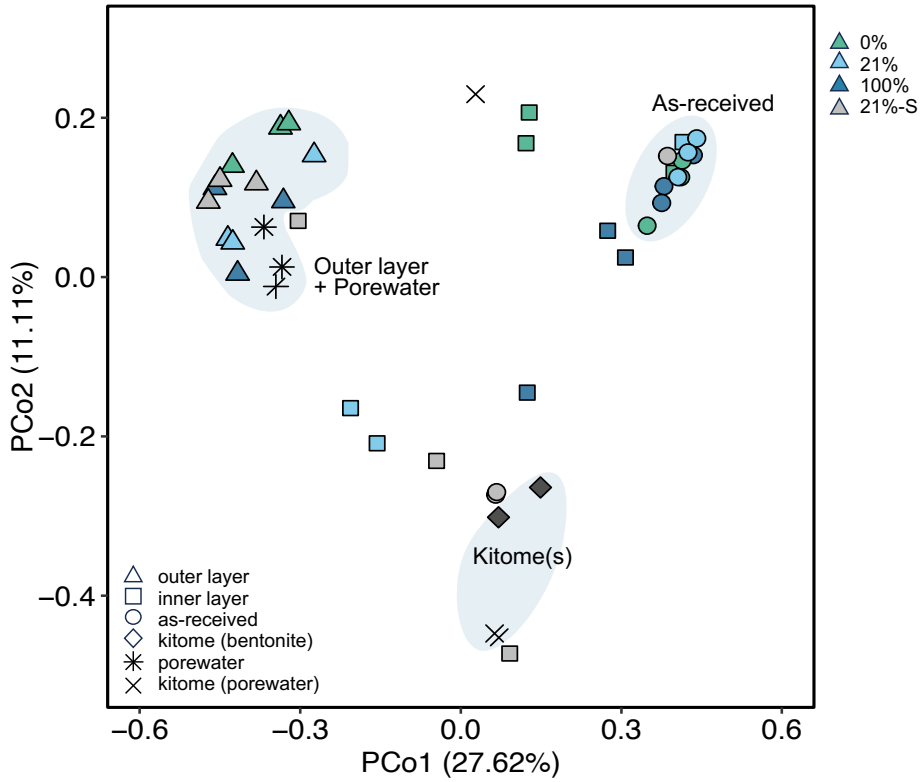

Figure S4. Principal Coordinate Analysis (PCoA) of 16S rRNA gene amplicon data for bentonite samples, porewater, as-received materials, and extraction kit controls (kitome). The inner and outer layer of the bentonite core is distinguished using different markers (see the legend). Different colors correspond to different concentrations of O_2 in the atmosphere used to equilibrate the samples.

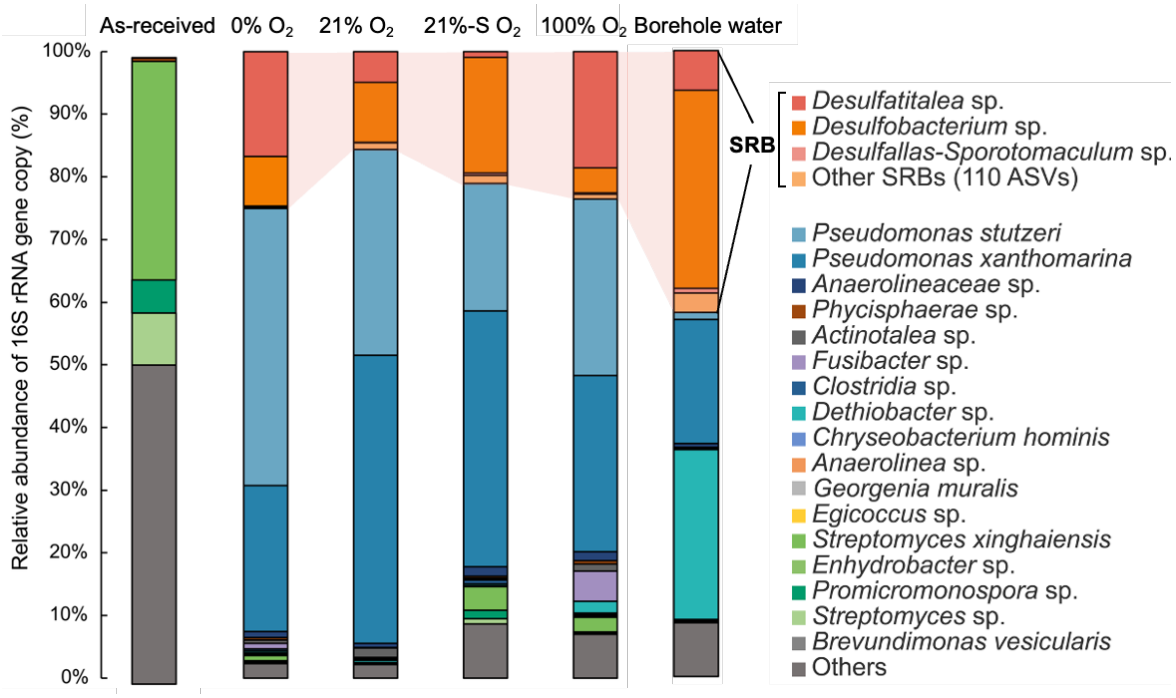

Figure S5. Microbial community composition based on full-length 16S rRNA gene amplicon sequencing representing borehole water, the outer parts of the bentonite core for each of the oxygen treatments, and as-received bentonite MX80. Species identified as sulfate-reducing bacteria (SRB) are shown in red-orange colors. The category 'Others' includes all amplicon sequence variants (ASVs) with an abundance of less than 2%.

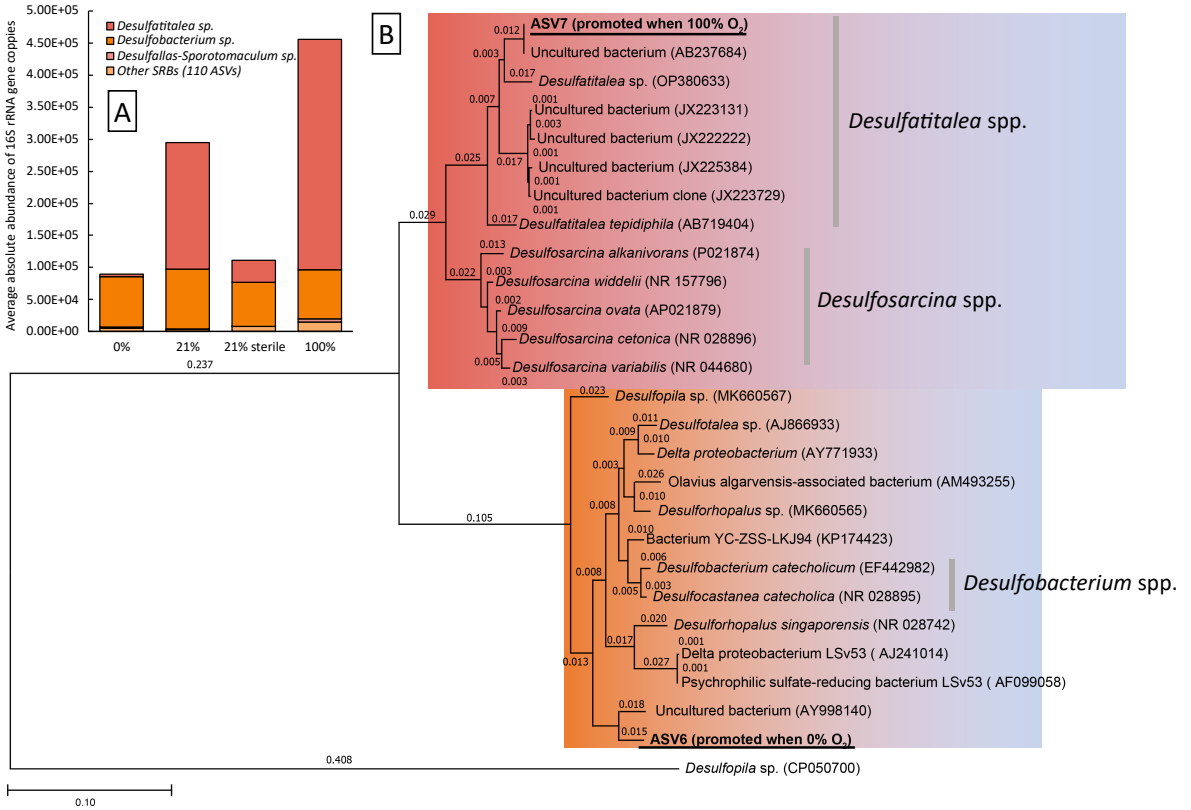

Figure S6. The absolute abundance **(A)** and taxonomy **(B)** of the two most abundant SRB: *Desulfurobacteriu*m sp (orange) and *Desulfatitalea* sp. (red) after 1.5 years of *in-situ* incubation in the borehole. The absolute abundance of 16S rRNA gene copies is represented by bars showing the average (3 samples for each treatment) SRB composition in the outer layer of the bentonite cores equilibrated with varying O_2 concentrations and the gamma-sterilized bentonite. The tree is constructed using maximum likelihood method. *Desulfopia* sp (CP050700), a common sulfate-reducing bacteria (SRB), was used as the outgroup.

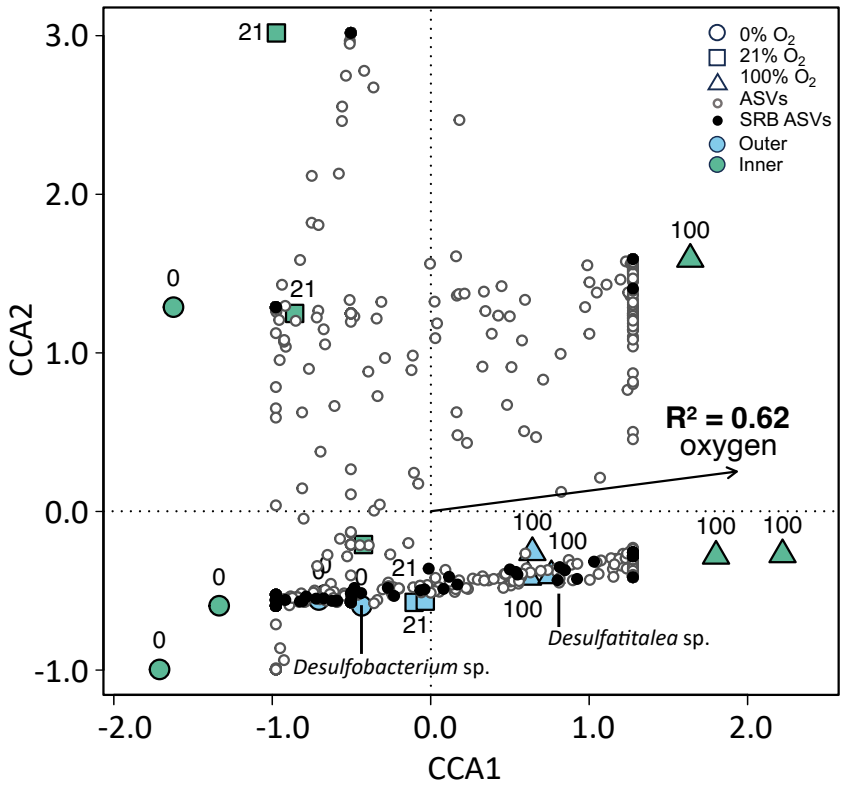

Figure S7. Canonical Correspondence Analysis (CCA) of microbial communities in bentonite, showing variation in relation to O_2 concentration to which bentonite was equilibrated before the deployment. Combined analysis of samples from both inner (green) and outer (blue) layers of the core. Shapes represent oxygen treatments: circles (0% O_2), squares (21% O_2), and triangles (100% O_2). Each small circle represents an ASV; sulfate-reducing bacteria (SRB)-related ASVS are shown in black, with the two most abundant SRBs labelled. The arrow indicates the direction and strength of the correlation between O_2 concentration and community composition. Oxygen has a stronger impact on the communities in the outer layer of the cores, which is indicated by the distribution of points representing ASVS and the difference in R^2 value when both outer and inner layer communities are included ($R^2 = 0.89$ vs. $R^2 =$, see Fig. 1).

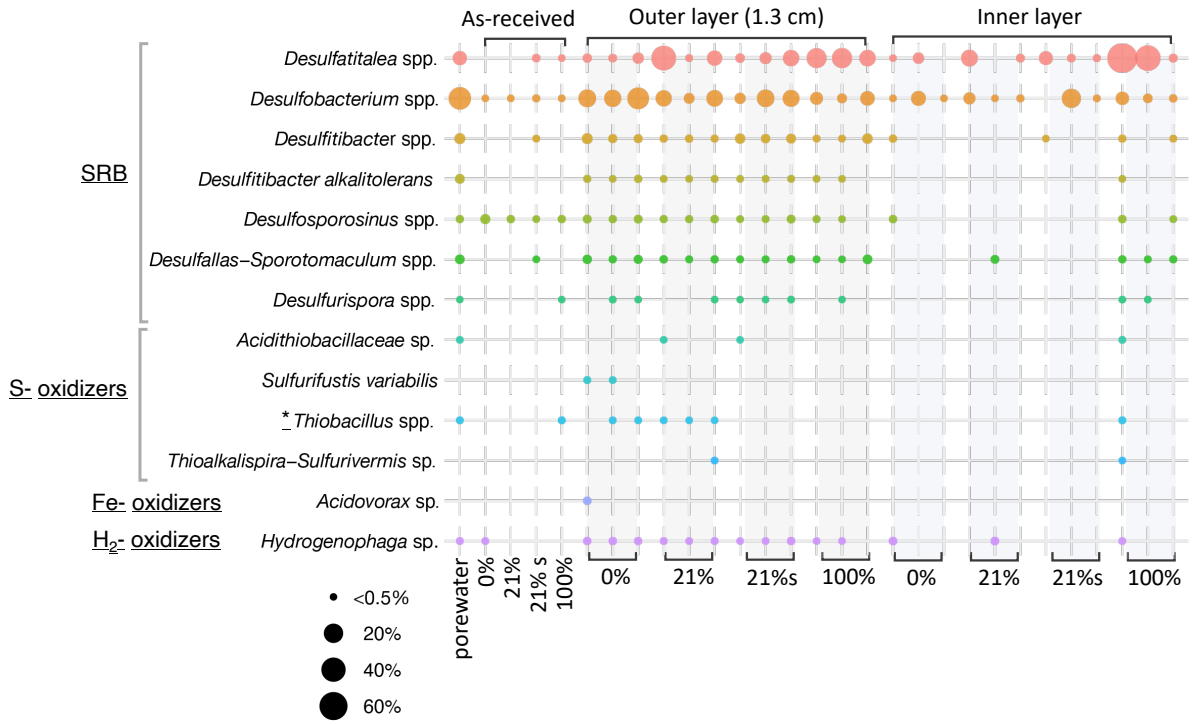

Figure S8. Bubble plot showing the relative abundance of ASV related to bacteria putatively metabolizing S-, Fe-species and H_2, identified in the as-received MX80 equilibrated to atmospheres varying in O_2 content (as-received bentonite), outer and inner bentonite layers. Different sizes of the bubbles correspond to varying abundance. *Thiobacillus* spp. are marked with (*), as they not only participate in S-oxidation but are also putative Fe(III)-reducers.

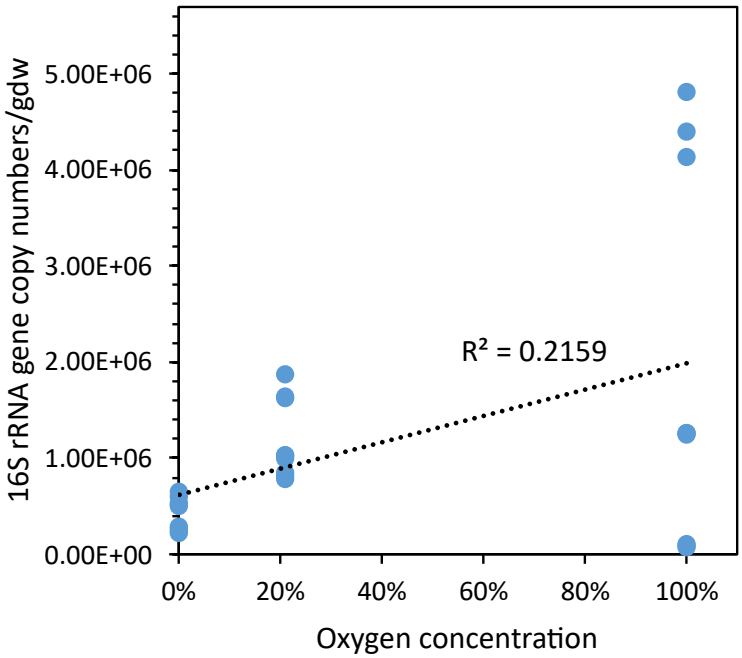

Figure S9. The distribution of 16S rRNA gene copy numbers normalized to grams of dry bentonite in relation to the oxygen concentration in the atmosphere used to equilibrate the bentonite prior to its deployment into the borehole. The dashed line indicates a positive linear correlation, with an R^2 value of 0.2159.

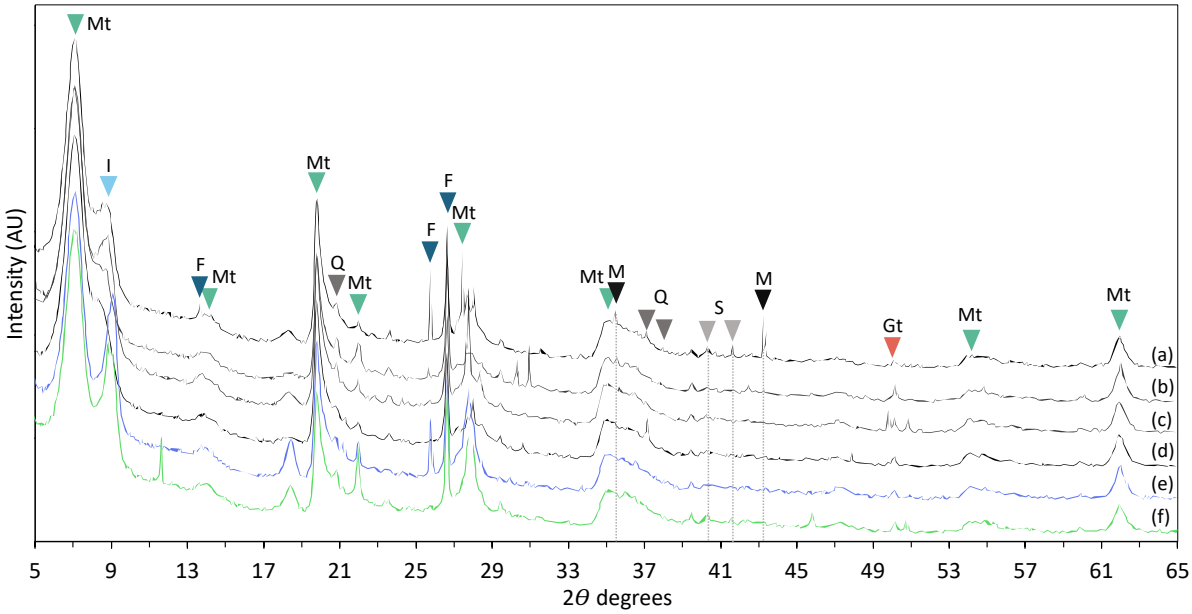

Figure S10. Powder X-ray diffraction patterns on the randomly oriented mounts. The patterns represent the outer layers of the bentonite cores: 0% 0_2 (a), 21-S% 0_2 (b), 21% 0_2 (c), 100% 0_2 (d), and the reference materials: as-received MX80 (e; blue line) and gamma-sterilized MX80 (f; green line). Triangles above the patterns represent characteristic peak positions of the minerals identified in the samples: montmorillonite (Mt), illite (I), feldspar (F), quartz (Q), and goethite (Gt) together with new mineral phases identified as magnetite (M) and siderite (S).

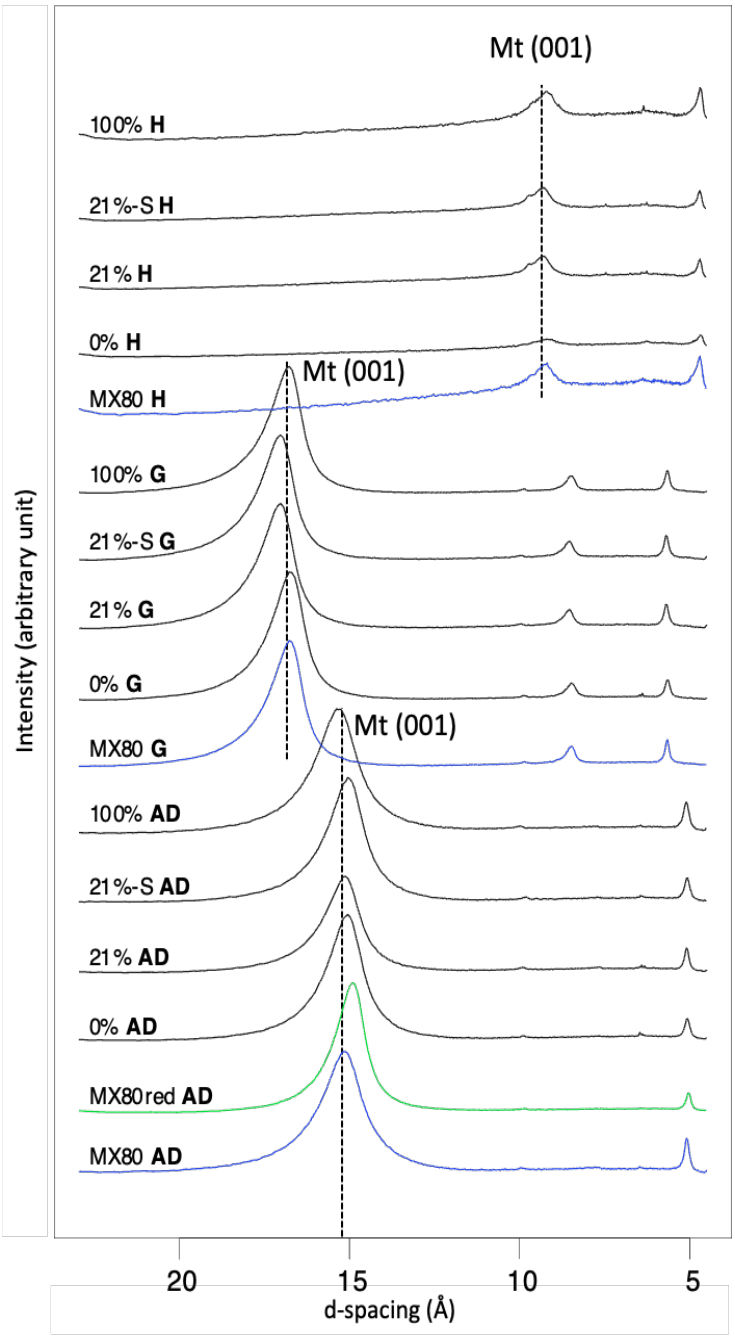

Figure S11. XRD patterns of oriented clay mounts following a step-procedure to identify clay minerals: air-dried (**AD**), expanded by ethylene glycol (glycolated; **G**), and heated (**H**) at 550°C. The dashed vertical line represents the position of the reflection from the basal 001 montmorillonite (Mt) plane. The samples also contain illite. The blue line represents untreated (as-received) MX80 bentonite. The green line represents MX80 bentonite chemically reduced with 30 mM Na_2S. No new clay phases were identified in the samples after the *in-situ* incubation.

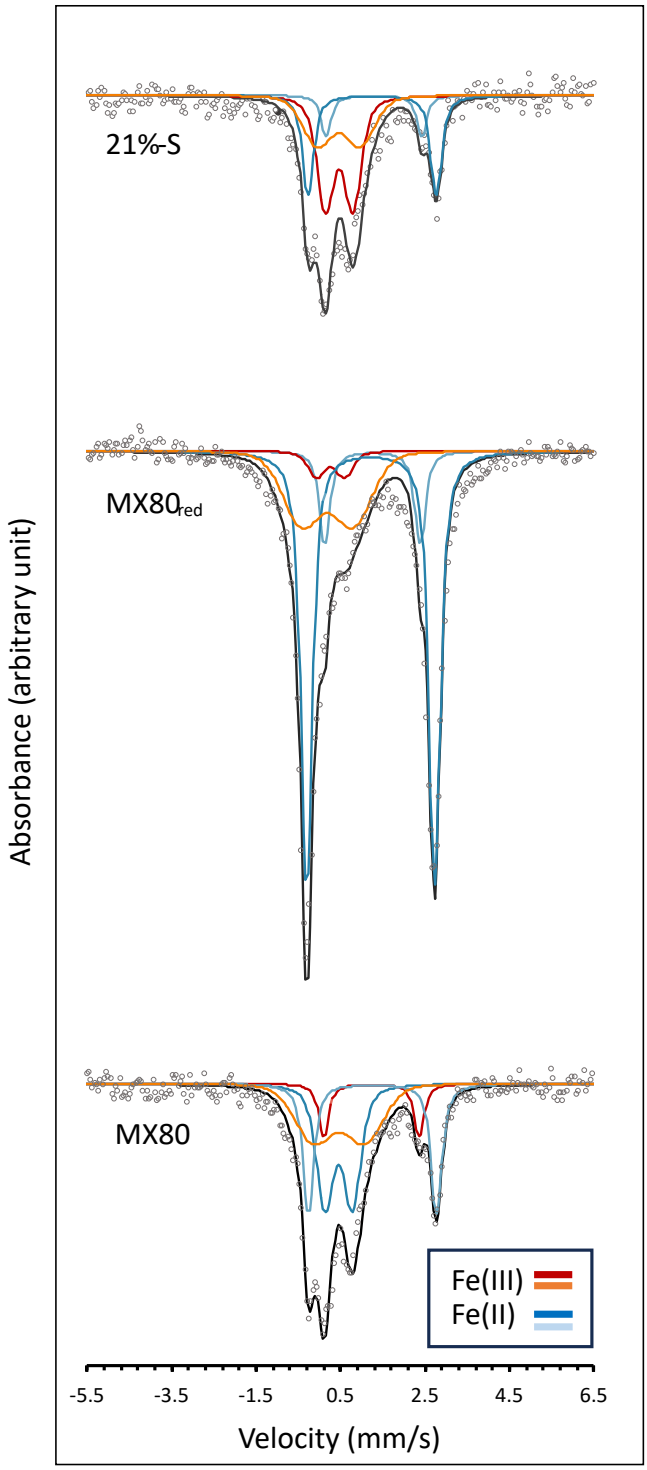

Figure S12. Mössbauer spectra (collected at 77 K) of two reference materials: as-received MX80 (MX80) and chemically reduced MX80 ($MX80_{red}$), and a gamma-sterilized bentonite sample equilibrated with 21% O_2 incubated *in-situ* incubation (21%-S). Empty circles represent raw data, while the black line shows the fitted spectrum. Blue lines represent fitted Fe(II) doublets, while orange-red lines correspond to fitted Fe(III) doublets.

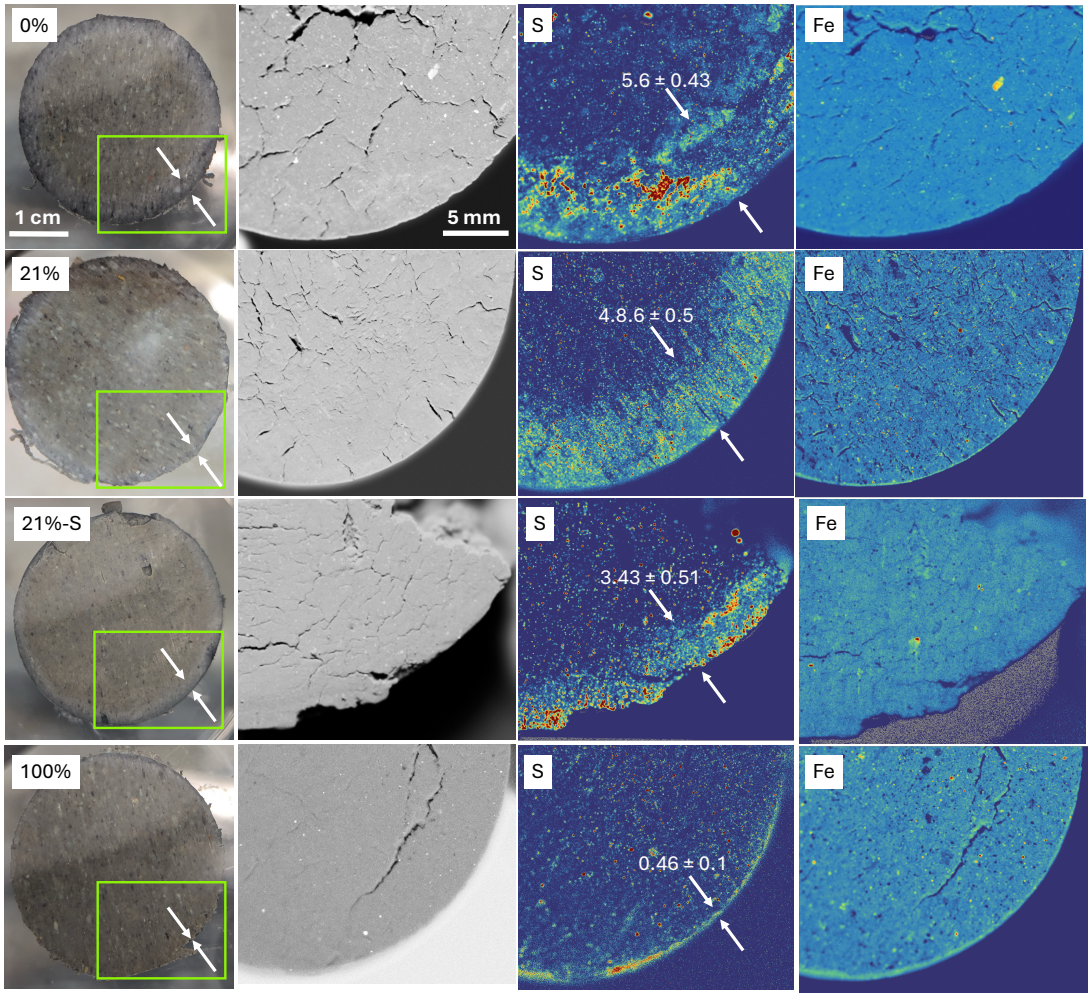

Figure S13. Macroscopic and microscopic pictures and XRF elemental distribution maps showing S and Fe distribution in the outer layer of the bentonite cores. Horizontal panels represent (from the top): 0% O_2, 21% O_2 gamma-irradiated (sterile), 21% O_2 and 100% O_2 bentonite treatments. Accumulation of S represented as the distribution of bright blue spots in the last column, differs between the treatments reflecting the sulfate reduction front within the bentonite and the contact with sulfate-containing

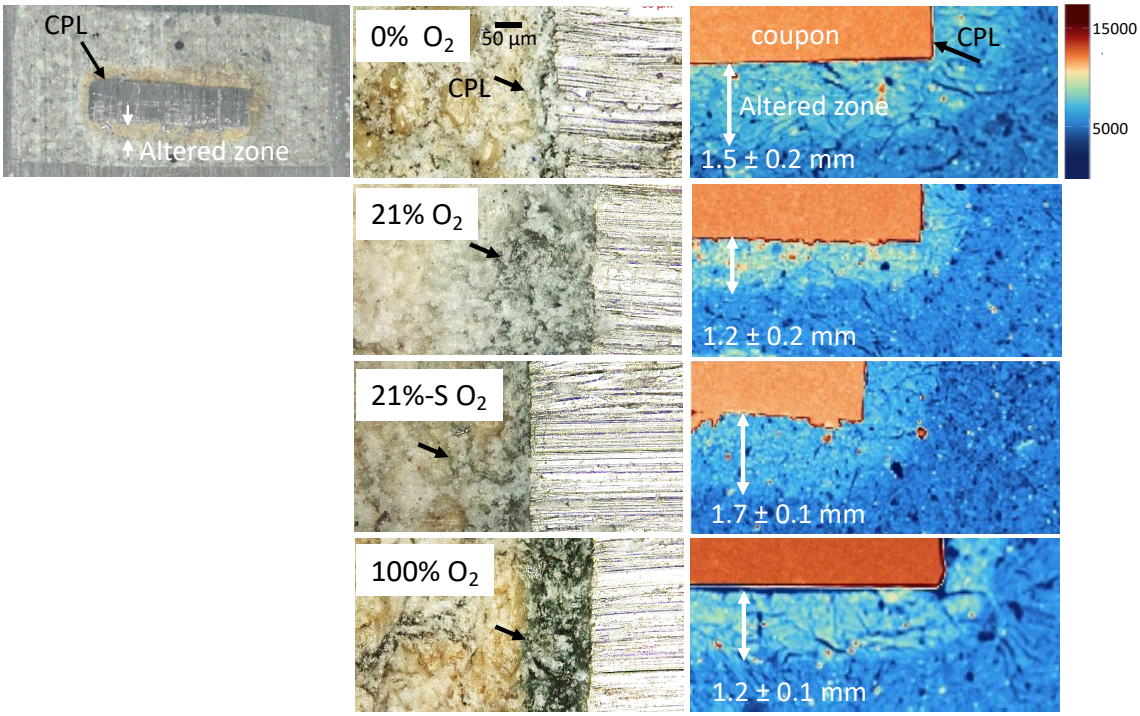

Figure S14. Confocal microscopy images and XRF maps illustrate the cross-sectional analysis of the resin-embedded coupon-bentonite interface. The black arrows indicate the Corrosion Product Layer (CPL), while the white arrows indicate the altered zone, with numerical values representing the TM thickness (n>15) in mm. Elemental distribution maps show iron (Fe) localization around the carbon steel coupon, with horizontal panels depicting different treatment conditions: 0% O_2, 21% O_2 and 21% O_2 gamma-irradiated (sterile), and 100% O_2.

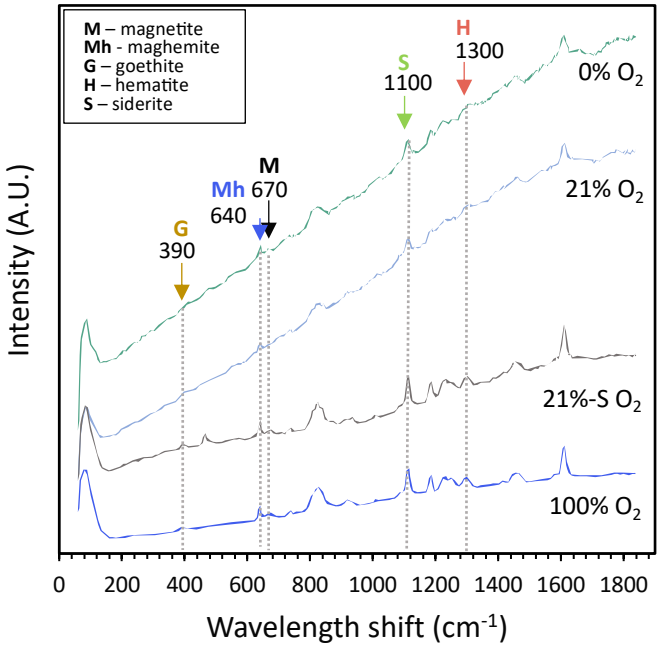

Figure S15. µRaman spectra of CPL showing corrosion product. Letters, arrows and dotted lines indicate the characteristic peak positions for magnetite (**M**), maghemite (**Mh**), goethite (**G**), hematite (**H**) and siderite (**S**) identified in the sample.

STEP 1: Saturation and bentonite swelling

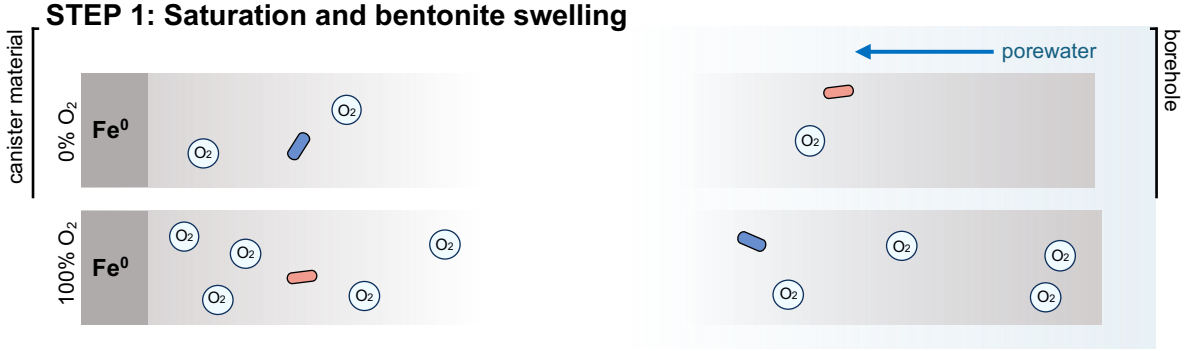

- Slow saturation, mainly diffusion-controlled.
- Indigenous bentonite bacteria are inactive.

- Partly advective flow, until the bentonite swells.

STEP 2: Oxic corrosion and bacterial colonization

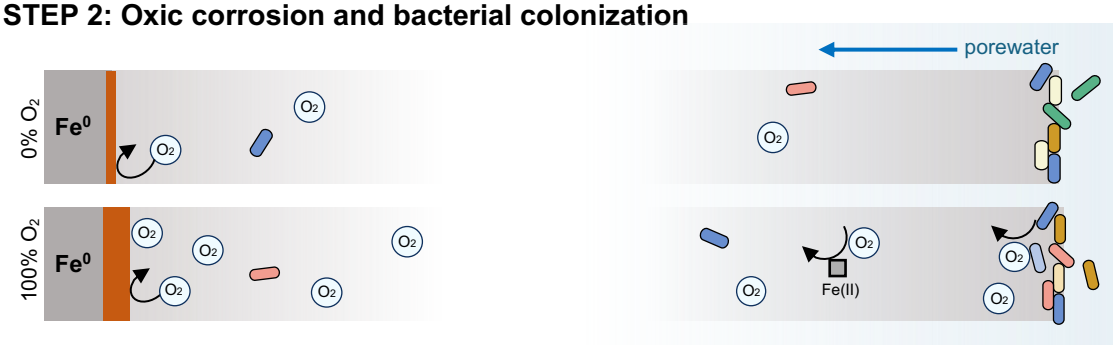

- Formation of primary Fe(III) (oxy)hydroxides (**oxic corrosion**) happens due to the abiotic reaction with O_2 and water present in the as-received bentonite.
- The smaller thickness at **0% O_2** results from less O_2 (trace amounts adsorbed to the bentonite).

- Porewater bacterial cells colonize bentonite until it fully swells (enough pore space)
- O_2 dissolves immediately in contact with porewater, leading to the formation of unique microbial assemblages. Biotic O_2 consumption.
- Abiotic O_2 depletion due to Fe(II)-phases oxidation.

STEP 3: Anoxic corrosion and sulfate reduction

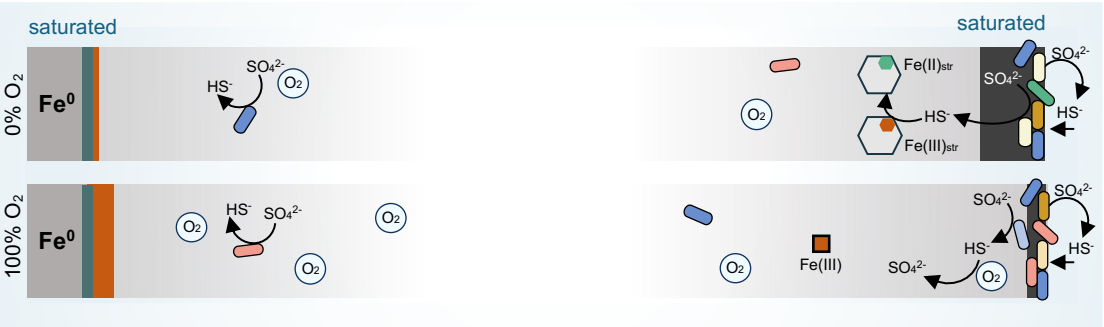

- Formation of Fe^{2+} through **anoxic corrosion** by the reduction of water and the production of H_2.

  ($Fe^0 \rightarrow Fe^{2+} + 2e^-$

  $H_2O + e^- \rightarrow OH^- + ½H_2\uparrow$).
- Locally, indigenous bentonite SRB reduce SO_4^{2-}.

- Activity of SRB. Production of HS^-. Potential activity of Fe(III)-reducing bacteria.
- Precipitation of mackinawite ($Fe_{1+x}S$).
- **100% O_2**: Smaller thickness of the $Fe_{1+x}S$ layer results from the re-oxidation of HS^-. In addition, the available Fe(II) to form $Fe_{1+x}S$ was depleted by residual O_2.
- **0% O_2:** Abiotic reduction of Fe(III), incl. $Fe(III)_{str}$ in montmorillonite by HS^-.

STEP 4: Corrosion product layer (CPL) formation

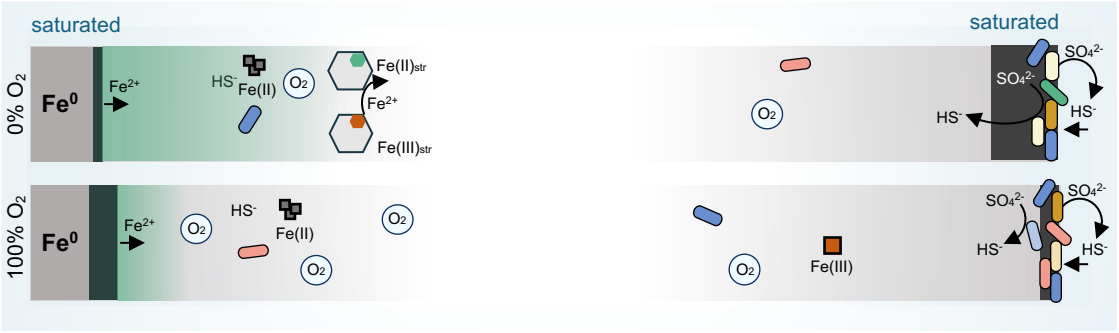

- Diffusion of Fe^{2+} into the clay through the primary Fe(III) (oxy)hydroxides layer.
- **CPL formation** via the transformation of Fe(III) (oxy)hydroxides into magnetite (e.g., Schikkor reaction).
- Continuous diffusion of Fe^{2+}. Precipitation of $Fe_{1+x}S$.
- **100% O_2:** Fe^{2+} travels a shorter distance as more is used to transform the thicker primary (oxy)hydroxides layer, and due to its slower diffusion rate through the forming CPL.
- If O_2 absent: the reduction of Fe(III) by Fe^{2+}.
- Continuous production of HS^- at the boundary with the host rock (porewater) if the porosity is sufficient to allow for bacterial activity.
- Diffusion of HS^- inside bentonite.

STEP 5: Altered zone formation

- **Altered zone formation:** oxidation of Fe^{2+} in contact with the residual O_2. Formation of Fe(III) (oxy)hydroxides.
- **100% O_2:** The shorter thickness of the zone is dictated by the distance Fe^{2+} could travel (see the previous step).
- Indigenous bentonite bacteria activity is limited, or they become inactive.
- Continuous production of HS^- at the boundary with the host rock (porewater) if the porosity is sufficient to allow for bacterial activity.
- Diffusion of HS^- inside bentonite.

Figure S16. Conceptual model depicting the formation of corrosion products of carbon steel and the microbial activity within bentonite. The upper panel illustrates samples equilibrated at 0% O_2, while the lower panel corresponds to samples equilibrated at 100% O_2. The schematics show two regions: the near-field, next to the canister material (left), and the far-field, represented by the bentonite in direct contact with porewater and the Opalinus Clay host rock.

3. Supplementary tables

Table S1. Fe chemical extraction data from bentonite samples using 0.5 M HCl, 6 M HCl and hydrofluoric acid (HF).

Solvent	Fe pool	0% O_2 mg/gdw[b]	21% O_2 mg/gdw	21% O_2-S mg/gdw	100% O_2 mg/gdw	MX80 mg/gdw	MX80-S mg/gdw	Na_2S-reduced[c] mg/gdw	$Na_2S_2O_4$ reduced[d] mg/gdw
0.5 M HCl	Fe(II)	1.88	2.16	1.95	2.42	1.81	1.48	15.63	16.10
	Fe(III)	0.00	0.00	0.00	0.00	0.00	0.00	0.00	0.00
	Total $Fe_{0.5M\ HCl}$[a]	1.88	2.16	1.95	2.42	1.81	1.48	15.63	16.10
6 M HCl	Fe(II)	8.62	6.72	6.57	5.12	3.31	2.80	14.07	14.49
	Fe(III)	4.20	0.70	1.89	2.40	3.85	5.22	0.00	0.00
	Total $Fe_{6M\ HCl}$[a]	12.82	7.43	8.45	7.53	7.17	8.02	14.07	14.49
HF	Fe(II)	10.32	7.00	5.47	4.97	2.58	n.d.	n.d.	n.d.
	Fe(III)	13.55	14.56	18.67	16.84	22.92	n.d.	n.d.	n.d.
	Total Fe_{HF}[a]	23.87	21.56	24.14	21.81	25.50	n.d.	n.d.	n.d.
HF	Fe(II)/Fe(III)	0.76	0.48	0.29	0.30	0.11	n.d.	n.d.	n.d.

[a]calculated as the sum of Fe(II) and Fe(III)
[b]mg per g of dry bentonite weight
[c]Wyoming MX80 bentonite chemically reduced with 30 mM Na_2S, elsewhere referred to as $MX80_{red}$
[d]Wyoming MX80 bentonite chemically reduced with 30 mM $Na_2S_2O_4$

Table S2. Mössbauer spectroscopy hyperfine parameters collected, including center shift (CS), quadrupole splitting (QS), hyperfine field (H), sigma, the relative area and the goodness of the fit χ^2.

§	Phase	CS (mm/s)	QS/ ε (mm/s)	H (T)	Σ	Relative area (%)	χ^2
MX80 (77K)	Fe(II) doublet	1.23	2.26		0.09	9.8	*1.16*
	Fe(II) doublet	1.26	3.03		0.12	25.6	
	Fe(III) doublet	0.46	0.65		0.29	33.5	
	Fe(III) doublet	0.47	1.25		0.72	31.1	
$MX80_{red}$[a] (77K)	Fe(II) doublet	1.24	2.26		0.12	12.0	*1.32*
	Fe(II) doublet	1.25	3.03		0.13	57.4	
	Fe(III) doublet	0.39	0.66		0.29	4.7	
	Fe(III) doublet	0.24	1.25		0.72	26.0	
0% (77K)	Fe(II) doublet	1.26	3.04		0.11	46.0	*0.88*
	Fe(II) doublet	1.24	0.28		0.09	5.4	
	Fe(III) doublet	0.44	0.63		0.25	26.8	
	Fe(III) doublet	0.45	1.02		0.56	21.8	
21% (77K)	Fe(II) doublet	1.29	2.26		0.09	9.2	*1.01*
	Fe(II) doublet	1.25	3.03		0.12	35.1	
	Fe(III) doublet	0.47	0.65		0.29	29.5	
	Fe(III) doublet	0.46	1.02		0.56	26.2	
21%-S (77K)	Fe(II) doublet	1.29	2.26		0.09	9.6	*0.83*
	Fe(II) doublet	1.25	3.03		0.12	24.9	
	Fe(III) doublet	0.47	0.65		0.29	38.6	
	Fe(III) doublet	0.46	1.02		0.56	27.0	
100% (77K)	Fe(II) doublet	1.40	2.26		0.09	9.0	*0.97*
	Fe(II) doublet	1.24	3.06		0.12	22.4	
	Fe(III) doublet	0.48	0.61		0.28	32.1	
	Fe(III) doublet	0.46	1.02		0.56	36.5	

[a]Wyoming MX80 bentonite chemically reduced with 30 mM Na_2S

Table S3. Data comparison between the relative percentage of total Fe(II) and total Fe(III) in the samples obtained by two different methods: hydrofluoric (HF) acid digestion Mössbauer spectroscopy. The sum of Fe(II) and Fe(III) was obtained by the addition of the respective relative areas of Fe(II) and Fe(III) listed in detail in Table S2.

	HF acid digestion		Mössbauer spectroscopy	
Sample	**Fe(II) (%)**	**Fe(III) (%)**	**Fe(II) relative area (sum; %)**	**Fe(III) relative area (sum; %)**
MX80	10.20	89.80	30.6	69.4
$MX80_{red}$[a]	n.d.	n.d.	51.4	48.6
0%	43.10	56.90	44.3	55.7
21%	32.41	67.59	34.5	65.5
21%-S	22.82	77.18	31.4	68.6
100%	22.94	77.06	35.4	64.6

[a]Wyoming MX80 bentonite chemically reduced with 30 mM Na_2S

Table S4. Corrosion of C-steel coupons inside compacted bentonite equilibrated with 0%, 21% and 100% O_2-containing atmosphere and in an anoxic borehole for 1.5 years. Abiotic control (gamma-sterilised bentonite) was equilibrated with a 21% O_2-containing atmosphere. The results represent the thickness of the corrosion product layer (CPL) and altered zone, mass loss over the course of 1.5 years of *in-situ* incubation and mass-loss corrosion rates per year.

Sample	**CPL thickness (µm)**	**Altered zone thickness (mm)**	**Mass loss (g)**	**Corrosion rate (µm/year)**
0% O_2	38.1±19.2	1.5±0.2	0.010	2.50
21% O_2	121.5±79.7	1.2±0.1	0.009	2.25
21%-S O_2	72.0±19.3	1.7±0.1	0.011	2.75
100% O_2	96.5±33.9	1.2±0.2	0.017	4.25

4. Supplementary references

(1) Pearson, F. J. *Opalinus Clay Experimental Water: A1Type, Version 980318*; Villigen PSI, Switzerland, 1998.

(2) Fredrickson, J. K.; Zachara, J. M.; Kennedy, D. W.; Dong, H.; Onstott, T. C.; Hinman, N. W.; Li, S. M. Biogenic Iron Mineralization Accompanying the Dissimilatory Reduction of Hydrous Ferric Oxide by a Groundwater Bacterium. *GeCoA* **1998**, *62* (19), 3239–3257. https://doi.org/10.1016/S0016-7037(98)00243-9.

(3) Heron, G.; Crouzet, C.; Bourg, A. C. M.; Christensen, T. H. Speciation of Fe(II) and Fe(III) in Contaminated Aquifer Sediments Using Chemical Extraction Techniques. *Environ Sci Technol* **1994**, *28* (9), 1698–1705. https://doi.org/10.1021/ES00058A023/.

(4) Poulton, S. W.; Canfield, D. E. Development of a Sequential Extraction Procedure for Iron: Implications for Iron Partitioning in Continentally Derived Particulates. *Chem Geol* **2005**, *214* (3–4), 209–221. https://doi.org/10.1016/J.CHEMGEO.2004.09.003.

(5) Stookey, L. L. Ferrozine-A New Spectrophotometric Reagent for Iron. *Anal Chem* **1970**, *42* (7), 779–781. https://doi.org/10.1021/AC60289A016.

(6) Amonetie, J. E.; Templeton, J. C. *Improvements to the Quantitative Assay of Nonrefractory Minerals for Fe(II) and Total Fe Using 1,10-Phenanthroline*; 1998; Vol. 46.

(7) Ilgen, A. G.; Kukkadapu, R. K.; Leung, K.; Washington, R. E. "Switching on" Iron in Clay Minerals. *Environ Sci Nano* **2019**, *6* (6), 1704–1715. https://doi.org/10.1039/C9EN00228F.

(8) Stucki, J. W. The Quantitative Assay of Minerals for Fe2+ and Fe3+ Using 1,10-Phenanthroline—II: A Photochemical Method. *Soil Sci. Soc. Amer. J.* **1981**, *45* (3), 638–641. https://doi.org/10.2136/sssaj1981.03615995004500030040x.

(9) Lagarec, K.; Rancourt, D. G. Extended Voigt-Based Analytic Lineshape Method for Determining N-Dimensional Correlated Hyperfine Parameter Distributions in Mössbauer Spectroscopy. *Nucl Instrum Methods Phys Res B* **1997**, *129* (2), 266–280. https://doi.org/10.1016/S0168-583X(97)00284-X.

(10) Rueden, C. T.; Schindelin, J.; Hiner, M. C.; DeZonia, B. E.; Walter, A. E.; Arena, E. T.; Eliceiri, K. W. ImageJ2: ImageJ for the next Generation of Scientific Image Data. *BMC Bioinformatics* **2017**, *18* (1). https://doi.org/10.1186/S12859-017-1934-Z.

(11) ASTM International. Standard Practice for Preparing, Cleaning, and Evaluating Corrosion Test Specimens. *Standard G1-03, ASTM Int., West Conshohocken, PA, USA.* **2017**.